Post-translational modifications of microtubules are crucial for malaria parasite transmission

Kodzo Atchou[1,2*], Magali Roques[1], Ruth Rehmann[1], Reto Caldelari[1], Melanie Schmid[1,2], Simone Grossi[1], Bianca Manuela Berger[1,2], Torsten Ochsenreiter[1], Friedrich Frischknecht[3], Volker Heussler[1*]

[1] Institute of Cell Biology, University of Bern, 3012 Bern, Switzerland

[2] Graduate School for Cellular and Biomedical Sciences, University of Bern, 3012 Bern, Switzerland

[3] Department of Parasitology, University of Heidelberg Medical School, Im Neuenheimer Feld 324, 69120, Heidelberg, Germany

***** Corresponding authors

Abstract

Microtubules, composed of α- and β-tubulin polymers, are essential components of the eukaryotic cytoskeleton. They maintain cellular shape and structural integrity and play critical roles in cell division and in intracellular vesicular transport. In *Plasmodium,* the parasite that causes malaria, nuclear replication during the liver stage is among the fastest known in eukaryotic cells and relies heavily on microtubules for DNA segregation and cytoskeletal organization. Despite their importance, the role of microtubules in liver stage development remains largely unexplored. Here, we investigated microtubule dynamics during liver stage development using a combination of cell and molecular biology techniques, expansion microscopy, and live-cell imaging. By employing antibodies specific for α-tubulin post-translational modifications (PTMs), we found that the *Plasmodium* sporozoites subpellicular microtubules (SSPM) persist during liver infection, giving rise to liver stage parasite microtubule bundles (LSPMB). These LSPMB form multimeric tubulin structures within hepatocytes and are redistributed to the hemi-spindle poles of parasite nuclei during schizogony. Deletion of the C-terminal region encompassing all known *Plasmodium* α-tubulin PTM sites prevented sporozoite migration from the mosquito midgut to the salivary glands, effectively blocking parasite transmission. Using *Plasmodium* microtubule-specific depolymerisation drugs, we found that while LSPMB are stable in sporozoites, they exhibit dynamic behavior during hepatocyte infection. Given the regulatory role of PTMs in microtubule dynamics, we generated parasite mutants by substituting and deleting key α-tubulin C-terminal residues involved in PTMs. Substitution of the polyglutamylation site with alanine and deletion of the C-terminal tyrosination/detyrosination motifs impaired parasite growth during liver infection. Together, our findings reveal extensive microtubule remodeling during liver stage development and establish α-tubulin C-terminal modifications as critical regulators of both intracellular development and parasite transmission of *Plasmodium* parasites.

Introduction

Plasmodium parasites are responsible for malaria and cause yearly half a million deaths in sub-Saharan countries. Malaria continues to be a major worldwide health concern despite recent successful attempts to lower its prevalence (1–4). The infection starts when an infected female *Anopheles* mosquito, during a blood meal, injects salivary gland sporozoites into the skin of the vertebrate host. Some of the motile sporozoites escape the host immune defence and invade blood vessels. They are carried by the blood flow to the liver, where they invade and infect hepatocytes (5). Approximately 50% of the parasites are often killed by host cell responses (6–8). Those that managed to establish a productive invasion form a parasitophorous vacuole (PV) in which the parasite undergoes massive growth and asexual replication known as schizogony. One single parasite gives rise to thousands of daughter parasites called merozoites in 3 to 6 days depending on the *Plasmodium* species (9–11). Fully developed merozoites exit the liver cells

in merosome vesicles through adjacent blood vessels (11–14). The merosomes then rupture and release merozoites into the blood stream. The parasites immediately invade erythrocytes, where they undergo again asexual replication to form the blood stage merozoites. Some merozoites differentiate into sexual stages, termed gametocytes, which are ingested by female mosquitos during a blood meal. In the mosquito midgut, the gametocytes develop into microgametes and macrogametes, which fertilize and form a zygote. The later undergoes differentiation into motile ookinetes, which penetrate the gut wall, forming oocysts (15–18). The oocyst produces the midgut sporozoites from the sporoblasts. The sporozoites migrate to the salivary gland from day 11 post-infection in *P. berghei* (Frischknecht et al., 2004; Frischknecht & Matuschewski, 2017; jerome P. Vanderberg, 1974; J. P. Vanderberg, 1975). During the liver stage development, the parasite relies on the fast and massive asexual replication which is essential for the transmission and pathogenesis in erythrocyte stage, representing key targets for malaria control strategies. Investigating the parasite microtubule dynamics during the rapid replication could provide important insight on the parasite biology and to develop strategies for halting the massive proliferation during the clinically asymptomatic liver stage.

Microtubules are cytoskeletal filaments of about 25nm outer diameter, made up of usually 13 chains of protofilaments composed of globular α-tubulin and β-tubulin heterodimers. They are crucial components of the cytoskeleton and offer structural support to cells and also function as tracks for the movement of organelles, vesicles, and other cellular components (23,24). Microtubules are involved in important cellular activities such as cell division and the production of cilia and flagella to allow cell motility. Microtubules exhibit inherent dynamics, alternating between polymerisation (rapid growth) and spontaneous depolymerisation (shrinkage) in a process termed dynamic instability (23,25,26). The dynamics of microtubules and their interactions with other cellular structures are regulated by specific microtubule-associated proteins (MAPs), which selectively bind to either the plus or minus ends of microtubules (27–30).

Tubulin is subject to seven identified post-translational modifications (PTMs), among which are acetylation of the lysine residue at position 40 in the luminally exposed part of α-tubulin, glycylation, which entails the incorporation of polyglycine side chains of variable length, phosphorylation, palmitoylation, tyrosination/detyrosination and polyglutamylation. These modifications are extensively preserved and enabling cells to modulate microtubule characteristics, dynamics, and interactions with microtubule-associated proteins (MAPs) and motor proteins (31,32). Tyrosinated microtubules are often associated with microtubule stability. These stable microtubules represent a specialised subset that exhibits enhanced resistance to depolymerization, even in the presence of destabilizing agents. They play a crucial role in maintaining cellular architecture, facilitating intracellular transport, and supporting specialized cellular functions. In contrast to dynamic microtubules, which continuously undergo cycles of polymerization and depolymerization due to dynamic instability, stable microtubules persist for extended periods. They are also frequently polyglutamylated, a modification that regulates their interactions with motor proteins and other cellular components. These microtubules are predominantly localized in structures requiring sustained structural integrity, such as cilia, flagella, neuronal axons, and motile cell types (33–36). Glutamylation, or polyglutamylation, is a post-translational modification characterized by the addition of multiple glutamate side chains to glutamate residues on both α- and β-tubulin. This modification occurs primarily at the C-terminal tails and is catalyzed by a family of enzymes known as polyglutamylases. Polyglutamylation plays a critical role in regulating the interactions of microtubules with MAPs and motor proteins, thereby influencing microtubule dynamics and cellular functions (37–40). The properties and functions of tubulin are largely encoded within their protein sequences, contributing to molecular diversity that influences key microtubule characteristics. This variation has been conceptualized as the "tubulin code", a regulatory framework through which cells control microtubule diversity to achieve specific physiological functions (24). Nevertheless, the precise mechanisms by which cells establish and interpret this code remain largely unknown. Although tubulin is highly conserved across evolution, it exhibits structural and functional variations between species, cell types, and even within single cells.

In eukaryotic cells, tubulins are key components of the microtubule cytoskeleton, and their genetic complexity reflects the organism's level of cellular specialization. In yeast, two distinct genes encode α-tubulin, while a single gene encodes β-tubulin. In contrast, the human genome contains nine genes encoding α-tubulin and an equal number encoding β-tubulin, reflecting a greater level of complexity and functional specialization in higher eukaryotes (24,41,42).

The *Plasmodium* genome encodes two α-tubulins (α1-tubulin and α2-tubulin) and one β-tubulin (43–47). The α1-tubulin gene encodes a protein of 450 amino acids, while α2-tubulin encodes 453 amino acids (48). The two isoforms share 94% amino acid identity. However, α2-tubulin lacks a terminal tyrosine residue, which is present in α1-tubulin. This difference suggests potential variation in post-translational modifications and functional roles (44,49). In *P. berghei,* the α1-tubulin gene is expressed across most stages of the *Plasmodium* life cycle, whereas α2-tubulin expression appears restricted to male gametocytes, gametes, and newly formed zygotes, indicating distinct functional roles for the two isoforms (32,50). Deletion of α1-tubulin blocks sporozoite formation in oocysts and lowering α1-tubulin expression leads to less infective sporozoites (50).

There is a significant degree of amino acid conservation between human and *Plasmodium* tubulins, with approximately 83.7% identity for α-tubulin and 88.5% for β-tubulin. However, *Plasmodium* tubulin shows greater similarity to plant tubulin than to mammalian tubulin. This raises the potential for developing compounds that selectively target parasite microtubules while sparing the host cell cytoskeleton, offering a promising avenue for therapeutic intervention (43,45–47,51).

Recent studies on *Plasmodium falciparum* blood stage schizonts have revealed that hemi-spindles lack polyglutamylation, whereas subpellicular microtubules do exhibit this post-translational modification (52–54). Similarly, SPMTs appear to be stabilized by microtubule inner proteins, while spindle microtubules do not show these luminal proteins (55). These differences may reflect functional specialisation of microtubule subpopulations in different cellular structures and developmental stages.

The liver stage of *Plasmodium* exhibits one of the fastest rates of replication known among eukaryotic cells, a process likely dependent on microtubule dynamics. However, to date, no studies have investigated microtubule dynamics during the liver stage. This study was therefore designed to explore the dynamics of parasite tubulin during the asexual liver stage, using recently developed expansion microscopy protocols (54,56–58).

Results

Expansion microscopy reveals the presence of the sporozoites subpellicular microtubules during the liver stage of infection

To investigate microtubule organization during the *Plasmodium* parasite liver stage, HeLa cells were infected with sporozoites and fixed them at different time points using cold methanol. We then performed IFA to stain host and parasite microtubules using an α-tubulin antibody (Figure 1A). The IFA revealed a marked accumulation of microtubules in proximity of the PVM (stained with anti-UIS4) from early infection (24 hours post-infection (hpi)) to the schizogony (30 to 54 hpi) (Figure 1A inlets). To examine these structures in greater detail, we applied the recently developed pre-staining expansion microscopy (PS-ExM) (56). By expanding the cells five-fold, PS-ExM enabled visualization of a large multimeric tubulin structure within the parasite, detectable from 6 hours post-infection (hpi) to 48 hpi (Figure 1B). Based on observations of sporozoites prior to liver infection, we hypothesize that this structure originates from the sporozoite subpellicular microtubules (SSPM) (Figure 1C top panel). We refer to this structure as the liver stage parasite microtubule bundles (LSPMB). Notably, the LSPMB progressively shrank over time and was no longer detectable by the end of schizogony (54 hpi) (Figure 1A, B). Using the 3D and 4D imaging software IMARIS, we quantified the LSPMB volume at various stages of liver infection. The results confirmed a consistent decrease in LSPMB size between 6 and 56 hpi (Figure 1D).

To verify that the LSPMB is not an artifact of the IFA and PS-ExM, we performed live cell imaging of infected HeLa cells. Cells were incubated with the tubulin tracker SPY650 for one hour prior to imaging. The LSPMB was clearly visible in sporozoites before invasion (Movie 1, ~10 hpi) and persisted until late liver stage development, gradually shrinking during schizogony (Figure 1E; Movies 2–4, ~36 hpi to 48 hpi). These live imaging results corroborate our findings from IFA and expansion microscopy, validating the presence and dynamic nature of the LSPMB during liver stage development.

The liver stage parasite subpellicular microtubules are dynamic

The SSPM has previously been described as highly stable structures, enabling sporozoite formation and invasion (50,55,59). These microtubules, similar to the corresponding microtubules in *T. gondii*, are resistant to conventional depolymerizing agents (59). To investigate whether the LSPMB retain this stability during liver stage development, we treated infected HeLa cells with the microtubule-depolymerizing agents Amiprophos-methyl (AMP) and oryzalin herbicide. These compounds are known to selectively target dynamic *Plasmodium* microtubules without affecting mammalian cells (43,45,47,51,60) (Figure 2 and Supplementary Figure 1A and B). We first validated drug specificity and cytotoxicity by testing various concentrations on HeLa cells over one week. Neither compound affected host cell viability (Supplementary Figure 1A and B) or disrupted host microtubules (Supplementary Figure 1Dand E). However, oryzalin showed a stronger inhibitory effect on parasite growth compared to AMP (Supplementary Figure C) and was therefore selected for further experiments (Figure 2A). Sporozoites were dissected into medium containing 10 µM or 20 µM oryzalin and then used to infect HeLa cells (Figure 2A and B), which were incubated with the same drug concentrations. At 48 hpi, the cells were fixed and analyzed by IFA and PS-ExM. To test reversibility, oryzalin was washed out at 24 hpi prior to the onset of schizogony (Figure 2B). At 10 µM, oryzalin significantly impaired nuclear replication, spindle formation, and LSPMB volume when present the entire cultivation time (Figure 2C, D and E). Partial recovery of hemi-spindles and nuclear replication was observed, suggesting that the effect of 10 µM oryzalin is reversible at this stage (Figure 2C, D, and E). However, at 20 µM, neither the hemi-spindles nor the LSPMB recovered after drug removal, indicating irreversible microtubule disruption at higher concentrations (Figure 2A and B). To investigate whether the microtubule depolymerization by oryzalin affects the parasite growth and survival during the liver stage, we measured parasite size within infected HeLa cells at 6, 24 and 48 hpi. Treatment with 10 µM oryzalin led to a significant reduction in parasite size and survival (Figure 2 F, G, H, and I). We further examined merozoite formation by staining for MSP1 at 56 hpi. Parasites treated with 10 µM oryzalin failed to express MSP1, indicating a block in merozoite development and suggesting that intact microtubules are essential for DNA replication and merozoite formation (Figure 2J). Interestingly, at lower concentrations of 0.5 µM, oryzalin treatment led to an unexpected elongation of the LSPMB and hemi-spindles up to four times longer than controls suggesting that microtubule turnover is tightly regulated (Supplementary Figure 1F, G and H). In conclusion, oryzalin-mediated depolymerization confirms that both the LSPMB and the hemi-spindles are dynamic structures during the liver stage. This dynamic behaviour was further supported by live-cell imaging using the SPY650 tubulin tracker (Movie 5, 6, and 7).

Given the observed microtubule remodeling in response to oryzalin, we next sought to determine whether known microtubule-associated proteins, specifically those regulating plus-end dynamics, are expressed during the liver stage and might contribute to the observed plasticity. Only a limited number of motor proteins and microtubule associated proteins, such as centrin and the kinesin protein family, have been identified during the *Plasmodium* liver stage (11,61–63). The recently characterized EB1 protein, known to regulate microtubules plus-end dynamics and length, has so far been reported for being expressed during the sexual blood stage (Mauer et al., 2023; Yang et al., 2023; Zeeshan et al., 2023). However, these studies did not assess EB1 expression during the asexual mosquito and liver stages. Given our observations of dynamic microtubule behavior and excessive polymerization following oryzalin treatment, we explored whether EB1 might be expressed during the liver stage. To this end, we generated a parasite line expressing endogenous

EB1 fused to eGFP via double homologous recombination (Supplementary Figure 2C and D). As expected, EB1-eGFP was detected in sexual blood stages (Supplementary Figure 2E and F) consistent with previous reports (64,65). Interestingly, we also observed EB1 expression in both midgut and salivary gland sporozoites (Supplementary Figure 2G). Importantly, EB1 was also detected during liver stage development, where it localized to the LSPMB and hemi-spindles (Supplementary Figure 2H–I).
These findings suggest that EB1 may play a broader role in *Plasmodium* microtubule regulation than previously recognized, potentially contributing to the dynamic remodeling of microtubules during the liver stage.

The liver stage parasite subpellicular microtubule carries tubulin post-translational modifications

Microtubule functions are often regulated by different post-translational modifications (PTMs), which influence their stability, interactions, and dynamics. To gain insight into the dynamic nature of LSPMB during the liver stage development, we examined α-tubulin PTMs using immunofluorescence (IFA) and expansion microscopy (Figure 3 and Movie 5, 6 and 7). To investigate whether the LSPMB is present in cell types other than HeLa cells, we infected primary hepatocytes with *Plasmodium* sporozoites and fixed the cells at different timepoints (6, 24, 36, 48, 54 and 56 hpi). We also analyzed sporozoites isolated from mosquito salivary glands. Using antibodies specific for polyglutamylated (anti-IN105) (66) (Figure 3A) and tyrosinated (anti-Ty) α-tubulin (Figure 3B), we observed that sporozoite microtubules, including the LSPMB, are both polyglutamylated and tyrosinated. Quantitative colocalization analysis confirmed a strong overlap between LSPMB and polyglutamylated tubulin in both sporozoites and liver stage parasites (Supplementary Figure 2A). Interestingly, following hepatocyte invasion, the LSPMB lost tyrosination (i.e., became detyrosinated) while retaining polyglutamylation. This detyrosination persisted throughout liver stage development, including early and late schizogony (24–56 hpi). During this period, polyglutamylation was observed on the LSPMB and at the poles of the hemi-spindles, but not along the polymerizing hemi-spindles themselves, which eventually disappeared along with the LSPMB (Figure 3A and C). Given previous findings implicating polyglutamylation in hemi-spindle pole formation in erythrocytic merozoites (31), we investigated whether there is a structural relationship between the LSPMB and the hemi-spindle poles. Using PS-ExM and the tubulin tracker SPY650, we visualized direct connections between LSPMB filaments and hemi-spindle poles. Live cell imaging confirmed this connection between LSPMB and hemi-spindle poles, mainly during the shrinkage of the LSPMB (Fig 3 F; Movie 8, 9 and 10, Supplementary Movie 1). These observations suggest that the LSPMB may be redistributed to form or support the hemi-spindle poles during schizogony. We also stained for γ-tubulin and observed its localization at the hemi-spindle poles in both the parasite and host cell (Supplementary Figure 2B), supporting the idea that *Plasmodium* may utilize γ-tubulin for nuclear division and microtubule assembly, as reported in other systems (67–70).
To further define the spatial localization of the LSPMB, we used *P. berghei* parasites expressing the plasma membrane protein PMP1 fused to superfolder GFP (sfGFP) previously generated (71). ImageJ RGB profiling revealed that the LSPMB lies between the parasite plasma membrane (PM) and the parasitophorous vacuole membrane (PVM), suggesting that the sporozoite subpellicular microtubules undergo subcellular relocalization during liver stage development (Figure 3D and E). At later stages, particularly the cytomere stage, we observed reappearance of tyrosinated tubulin near the parasite nuclei (Figure 3B). During merozoite formation, this tyrosinated tubulin appeared as punctate structures within the forming merozoites (Figure 3B).
Tyrosination has previously been associated with stable microtubules involved in motility, such as those in sporozoites, flagella, and spermatozoa (33,34,50,55). The absence of tyrosination during early intracellular liver stage development when the parasite is non-motile may facilitate its transformation from a banana-shaped sporozoite to a rounded liver stage form (Figure 1 and 3). LSPMB detyrosination may contribute to microtubule dynamic instability, providing both energy and tubulin monomers for rapid growth and spindle

formation during schizogony. Finally, the reappearance of tyrosinated microtubules during merozoite formation may serve to stabilize the microtubules required for merozoite motility and erythrocyte invasion.

The *Plasmodium* α-tubulin C-terminal modification are important for sporozoite formation

To investigate the functional role of parasite α-tubulin PTMs during the liver stage development, we generated *P. berghei* mutant parasite lines with targeted mutations in the α-tubulin C-terminal region, where most PTMs are predicted to occur (Figure 4A and Supplementary Figure 3A and B). Specifically, we created three mutant lines: PsΔ: a point mutation replacing the polyglutamylation site glutamic acid (E445) with alanine (A), TyΔ: deletion of the tyrosination/detyrosination motif (YEADY) from position 449, CtΔ: deletion of the entire C-terminal tail (EGEDEGYEADY) to prevent all possible C-terminal tail PTMs (Supplementary Figure 3A to C).
Using AlphaFold predictions, we confirmed that the mutations were unlikely to affect tubulin folding (Supplementary Figure 3C). The mutants were generated via double homologous recombination and verified by integration PCR and sequencing of the mutated α-tubulin gene (Figure 4A and B; Supplementary Figure 3B). The development of mutant parasites was investigated during the mosquito, and liver stages. Significant defects emerged during mosquito stage development. The PsΔ and TyΔ mutants were able to form oocysts (Figure 4 C, Supplementary Fig 4A) and gliding sporozoites, albeit in reduced numbers (Figure 4D, E and G; Supplementary Fig 4B; and Supplementary Movie 2, 3, 4 and 5). Quantification of salivary gland sporozoites at 18 days post-blood feeding showed that PsΔ and TyΔ mutants produced approximately half as many sporozoites as the control line (NoΔ) (Figure 4D). We next examined sporozoite motility, which typically consists of continuous circular gliding (16,72–76). PsΔ and TyΔ salivary gland sporozoites were assessed and compared to controls. While PsΔ have a similar gliding velocity compared to controls, TyΔ sporozoites displayed increased gliding velocity (2.5 µm/s vs. 1.4 µm/s) (Figure 4G), suggesting a regulatory role of the tyrosination motif in fine-tuning motility. To assess whether these motility phenotypes influenced infectivity, we performed in vivo infection assays with PsΔ and TyΔ. All mutant lines sporozoites were able to infect mice similarly to control parasites (Supplementary Figure 4C). However, the CtΔ mutant failed to produce salivary gland sporozoites entirely (Figure 4D). Since CtΔ mutant parasites failed to reach the salivary glands, we analyzed hemolymph sporozoites for this line compared to the controls (Figure 4F). These showed severely impaired motility, lacking the typical gliding pattern and exhibiting significantly reduced speed (Figure 4F and H). Given that PsΔ and TyΔ mutants produced motile salivary gland sporozoites, we infected HeLa cells with PsΔ and TyΔ mutant sporozoites and CtΔ mutant hemolymph sporozoites to assess their liver stage development and identify any downstream phenotypic effects.

The *Plasmodium* α-tubulin C-terminal mutants undergo liver stage development

Using polyglutamylation-specific antibodies, we found that PsΔ mutant parasites still exhibited polyglutamylated liver stage parasite microtubule bundles (LSPMBs) in both sporozoites and liver stage forms, although the signal intensity was significantly reduced compared to controls (Figure 5A, B and C and G). As tyrosination was previously observed only in sporozoites and late liver stages, we performed PS-ExM on sporozoites and stained them with α-tubulin tyrosination-specific antibodies. TyΔ salivary gland sporozoites and CtΔ hemolymph sporozoites both showed detectable tyrosination signals, although the signal in CtΔ parasites was markedly weaker than in controls (Figure 5D, E and F). Interestingly, as PTM-specific antibodies continued to recognize signals in the PsΔ and TyΔ mutants, it is possible that the parasite compensates by relocating the PTM sites to adjacent residues within the C-terminal sequence. Alternatively, the antibody signal may stem from β-tubulin modifications rather than α-tubulin.
To assess parasite survival and growth during liver stage development, we performed quantitative microscopy (Figure 5H to O). Both PsΔ and TyΔ mutant parasites successfully infected HeLa cells and progressed through liver stage development (Figure 5B, D, H, I, J and K). This was further confirmed by

staining the parasitophorous vacuole membrane (PVM) using anti-UIS4 antibodies (Figure 5A, B and C). Parasite size was measured at 6 hpi and 48 hpi to assess developmental progression. No significant differences were observed at 6 hpi (Figure 5I). However, by 48 hpi, mutant parasites were significantly smaller than controls, indicating impaired growth (Figure 5J). Survival rates of PsΔ and TyΔ mutants were comparable to controls (Figure 5K), with infection rates of 15% for PsΔ (matching the control) and 27% for TyΔ, exceeding the control. As expected, the CtΔ hemolymph sporozoites failed to infect and to develop liver stage forms (Figure 5C, L, M, N and O). The sporozoites failed to establish productive infections with a typical PVM at all examined time points (Figure 5C, M, N and O).

To confirm the phenotypes, we compared our mutants with previously generated *P. berghei* α1-tubulin mutants described by Spreng et al. (2019), including parasites with intron deletions (intronΔ), C-terminal tyrosination deletions 540ADY (C-termΔ), and α2-tubulin exon swaps. These mutants showed similar phenotypes, including a complete absence of salivary gland sporozoites in α2-tubulin exon swap parasites, mirroring the CtΔ mutant phenotype (Figure 4D and H; Supplementary Figure 3D and E). These results underscore the importance of α-tubulin C-terminal PTMs in sporozoite formation and migration from the midgut to the salivary glands.

The failure of CtΔ parasites to generate viable sporozoites highlights the essential role of α-tubulin PTMs in sporozoite development and migration. Co-mutation of both α- and β-tubulin PTM sites may prove lethal to parasite development in the mosquito stage. Future studies should focus on identifying and characterizing the enzymes responsible for tubulin PTMs in *Plasmodium*, and genetic knockout strategies should be pursued to further elucidate the function of these modifications.

Discussion

Our study provides the first in-depth characterization of microtubule architecture and dynamics during the *Plasmodium* liver stage. Using tubulin trackers and α-tubulin antibodies, we identified two major microtubule populations: a large, multimeric subpellicular network that we termed the liver stage parasite microtubule bundles (LSPMB), and the polymerizing hemi-spindles involved in nuclear division. The LSPMB appears to originate from the SSPM and persists until late schizogony. These observations align with earlier electron microscopy studies by Meis et al. (77) who reported the presence of subpellicular microtubules and inner membranes in liver stage parasites up to the point of mitotic spindle formation.

The behavior and function of microtubules are closely regulated by PTMs. We found that α1-tubulin expressed during the liver stage carries residues associated with polyglutamylation and tyrosination. Using PTM-specific antibodies, we confirmed that *Plasmodium* sporozoites display both modifications on their subpellicular microtubules. Tyrosination, a well-known marker of stable microtubules, has been described in highly motile systems such as cilia, flagella, and spermatozoa (33,34,50,55). This is consistent with the need for high motility in sporozoites, which must traverse multiple tissue barriers during transmission (16,72,73).

Polyglutamylation, in contrast, introduces negative charges on the tubulin surface that enhance interactions with MAPs, and is commonly associated with dynamic microtubule behavior (78–80). This modification has previously been linked to merozoite formation and intracellular trafficking in *Plasmodium* blood stages (31). The co-occurrence of tyrosination and polyglutamylation in sporozoites likely ensures a microtubule network that is both stable and functionally interactive during mosquito stage migration.

Upon hepatocyte invasion, we observed a loss of tyrosination while polyglutamylation was maintained, suggesting a functional switch from stable to dynamic microtubules (Figure 6). This transition may facilitate morphological transformation from a motile, slender sporozoite into a rounded liver stage form and could also support the parasite's rapid replication. The liver stage is one of the fastest-replicating phases in the *Plasmodium* life cycle, with replication rates among the highest observed in eukaryotic cells (81,82). During this phase, the parasite synthesizes proteins de novo and hijacks host cell lipids and proteins for membrane biogenesis (83–86). We propose that the parasite brings its SSPM into hepatocytes to be

327 repurposed as the LSPMB (Figure 6). The observed microtubule disassembly over time may support tubulin
328 turnover and safes energy for intracellular development.
329 In addition to their structural roles, LSPMB filaments were occasionally found in contact with hemi-spindle
330 poles, suggesting that LSPMB contribute to spindle formation during schizogony. This connection, although
331 infrequent in fixed cells, was frequently observed during live imaging suggesting a transient connection. We
332 also detected expression of EB1, a microtubule plus-end binding protein previously believed to be restricted
333 to the sexual blood stage (64,65,87), during mosquito and liver stages. Its localization to LSPMB and hemi-
334 spindles suggests a broader role for EB1 in regulating microtubule dynamics throughout the parasite life
335 cycle.
336 To directly test the function of tubulin PTMs, we generated *P. berghei* mutants with targeted C-terminal
337 modifications of α1-tubulin. These included a glutamate-to-alanine substitution at a polyglutamylation site,
338 deletion of the tyrosination motif, and complete deletion of the C-terminal tail. Despite the mutations, PTM-
339 specific antibody staining remained detectable in the first two mutants, suggesting compensatory
340 mechanisms such as modification of adjacent residues or of β-tubulin. The tyrosination antibody used (anti-
341 Ty, T9028, Sigma-Aldrich) is a purified monoclonal antibody targeting C-terminal tyrosine residues on
342 tubulins, whereas the monoclonal GT335 antibody (AG-20B-0020-C100, AdipoGen Life Sciences)
343 recognizes the epitope formed at the branching point of polyglutamylation side chains (GEGE*EE, * marking
344 the modification site) and detects both short and long glutamate side chains. The polyclonal antibody (AG-
345 25B-0030-C050, AdipoGen Life Sciences) was raised against at least three glutamate residues and is
346 thereby specific to long polyglutamylation side chains, though both antibodies may cross-react with β-
347 tubulin or other proteins containing genetically encoded C-terminal modifications (66,88). The reduced
348 fluorescence signal observed (Figure 5) in mutant parasite microtubules suggests either antibody cross-
349 reactivity with β-tubulin or compensatory PTM relocation to adjacent α-tubulin residues. In the CtΔ mutant
350 (lacking the entire C-terminal tail), PTM relocation is abolished, and residual signal likely stems from β-
351 tubulin which was insufficient to sustain sporozoite motility and transmission. These possibilities warrant
352 further investigation. Previous studies have also demonstrated partial redundancy between α1- and α2-
353 tubulin modified (49,50,89). However, the complete C-terminal deletion mutant failed to produce salivary
354 gland sporozoites and could not establish liver stage infection. These results are consistent with findings
355 from Spreng et al. (2019), who showed that α1-tubulin mutants lacking the C-terminal region produced
356 defective sporozoites with altered microtubule numbers and impaired motility.
357 We also observed that the LSPMB relocates during liver stage development. Using expansion microscopy
358 on PMP1::GFP-expressing parasites (71), we found that the LSPMB localizes between the parasite plasma
359 membrane and the PVM. This differs from earlier reports of SSPM positioning (77,90–92) but both notions
360 are not mutually exclusive. It is possible that the LSPMB first localizes within the parasite but then re-
361 localizes at later stages or even re-localizes dynamically. Its localization between the PM and the PVM
362 positions it well for interaction with the host cell indicating an interaction with host cell structures such as
363 ER tubules or host microtubules (71,84,93,94). However, whether this re-localization plays a role in nutrient
364 acquisition or host-pathogen signaling remains to be explored.
365 Finally, during late schizogony and merozoite formation, we observed the reappearance of tyrosinated
366 tubulin. This may reflect the need for stable microtubules in newly formed merozoites, which must be
367 competent for host cell invasion.
368 In conclusion, our study reveals a previously unrecognized complexity in the microtubule biology
369 of *Plasmodium* liver stages. The identification of the LSPMB as a dynamic structure regulated by tubulin
370 PTMs and repurposed from the sporozoite cytoskeleton opens new avenues for understanding how the
371 parasite controls its intracellular architecture. These PTMs appear critical for parasite shape, replication,
372 and stage transition, and may represent valuable targets for therapeutic intervention. Future work should
373 aim to identify the enzymes responsible for these modifications and explore their potential as drug targets.
374 The behavior and function of microtubules are closely tied to their PTMs. We found that α1-tubulin
375 expressed during the liver stage carries residues predicted to undergo polyglutamylation and tyrosination.

376 Using PTM-specific antibodies, we confirmed that sporozoite microtubules are both tyrosinated and
377 polyglutamylated. Tyrosination is typically associated with stable microtubules and has been described in
378 highly motile structures such as cilia and spermatozoa. This is consistent with the sporozoite's need for
379 high motility gliding at approximately 1.5 µm/s as it migrates from the mosquito midgut to the salivary glands
380 and eventually traverses skin and vasculature to reach hepatocytes.

381 **Methods**

382 **Ethics statement**

383 All experimental procedures were performed in full compliance with the Swiss Animal Protection Act
384 (TSchG) and were approved by the Canton of Bern's Animal Experimentation Commission (Authorization,
385 BE118/22). Personnel involved in animal studies held the Federation of European Laboratory Animal
386 Science Associations (FELASA) accredited certifications. Female C57BL/6 and BALB/c mice of 6 to 10
387 weeks old and 20-30 g at infection were sourced from Janvier Labs (France) or bred in the animal facility
388 at the University of Bern's Institute of Cell Biology. Animals were maintained under standard housing
389 conditions with daily health monitoring by trained staff.

390 ***P. berghei* lines used in this study and the generation of transgenic parasites**

391 The *P. berghei* ANKA parasite line was utilized for both murine and cellular infection models. To generate
392 the α1-tubulin C-terminal mutant and eb1::eGFP parasite lines, the C-terminal coding and 3' untranslated
393 regions (UTRs) were cloned into the double homologous recombination vector pDHR, which contains the
394 3'UTR PbDHFR, the ef1α promoter region, the selectable markers hdhfr::yfcu, and additional 3'UTR
395 PbDHFR sequences. The pDHR vector backbone originated from the plasmid pG362 (kindly provided by
396 the Waters lab) (95).
397 First, the pG362 plasmid was digested with SacII and PstI to remove the AID, selectable marker, and GFP
398 sequences. The amplified product (linker-eGFP-3'UTR PbDHFR) from the pOB277 vector was then cloned
399 using T4 DNA ligase (NEB, M0202L). For subsequent cloning, restriction sites were added to the forward
400 (KpnI and ApaI) and reverse (EcoRI and SmaI) primers. The plasmid was then digested with EcoRI and
401 SmaI to clone the amplified product: ef1α promoter region-hdhfr::yfcu marker (a fusion gene of the positive
402 selection marker human dihydrofolate reductase (hdhfr) and the negative selection marker yeast cytosine
403 deaminase-uridyl phosphoribosyl transferase (yfcu) 3'UTR PbDHFR from the genomic DNA of the *P.*
404 *berghei* GIMO parasites (RMgm-687) parental line (96).
405 The complete α1-tubulin gene sequence (PBANKA_0417700), including 5' and 3' UTRs, was retrieved from
406 PlasmoDB (https://plasmodb.org). The linker-eGFP region of the pDHR vector was removed using ApaI
407 and NotI restriction enzymes. The 5'UTR of the α1-tubulin gene was then subcloned into the digested pDHR
408 using Gibson assembly. The resulting vector was digested with SmaI, and the PbHsp70 promoter and
409 mCherry regions from RMgm-687, along with the 3'UTR of the α1-tubulin gene, were subcloned into the
410 vector at the ApaI and SmaI restriction sites, respectively, using Gibson assembly.
411 Site-directed mutagenesis (QuickChange II XL Kit) was used to introduce the C-terminal modifications, with
412 primer sequences listed in Tables 2 and 3. The final plasmid was linearized with ScaI before being
413 transfected into the PbWT line (*P. berghei* ANKA line cl15cy1) (97). Similarly, the end-binding protein eB1
414 (PBANKA_0405600) with an eGFP tag was engineered using identical cloning strategies. The 5' and 3'
415 UTRs were retrieved from PlasmoDB (https://plasmodb.org) and subcloned into the pDHR vector at the
416 ApaI and SmaI restriction sites, respectively, using Gibson assembly. The final vector was linearized with
417 NdeI before being transfected into the Pb1868 line (constitutively expressing Hsp70-mCherry-ef1α-NLuc)
418 (98). Primer sequences are listed in Table 1.
419 Vector transfections were performed in schizont cultures as previously described (16,99). Briefly, *P. berghei*
420 schizonts were cultured and purified (16,99,100). Electroporation of schizonts from the respective parasite

421 lines was performed using the Amaxa® Human T Cell Nucleofector® system with the U33 program,
422 followed by intravenous injection into naïve mice. The construct was integrated by double-crossover
423 homologous recombination at the locus of interest. Pyrimethamine drug selection was administered via
424 drinking water, and parasitemia was monitored daily from day 7 post-infection until mice tested positive
425 (99).

426 **Parasitaemia measurement and cloning of transgenic parasite lines**

427 To measure the parasitemia ratio of infected mice, approximately 2 µL of blood from the tail vein of each
428 infected mouse was added to 500 µL of PBS and analyzed by flow cytometry using the NovoCyte (Agilent,
429 2023) as described (101). The data were analyzed using NovoExpress Flow Cytometry Analysis Software
430 (version 1.6.2, Build 230717.50551; Agilent Technologies).
431 To clone the different engineered transgenic parasite lines, mice were infected with the transgenic
432 parasites. Three days post-infection, parasitemia was assessed and when parasitemia reached at least
433 1%, blood was collected from the infected mouse via heart puncture following euthanasia as described
434 (16). The collected blood was passaged into a new naïve mouse. When parasitemia in the newly infected
435 mouse reached 1-2%, 2 µL of tail vein blood was collected and mixed with RPMI-1640. Maintaining low
436 parasitemia was crucial to prevent both double erythrocyte infection by *P. berghei* and gametocyte
437 formation. Single *P. berghei*- infected erythrocytes were then sorted into individual wells of 96-well plates
438 (Cellvis) containing 200 µL of RPMI-1640 supplemented with 10% FCS using a BD FACSDiscover S8 with
439 CellView. Supplementing the medium with 10% FCS allowed the sorted infected erythrocytes to recover
440 from the sorting process. Five mice were then intravenously infected with a single sorted infected
441 erythrocyte each. The mice underwent drug selection via drinking water, and parasitemia was monitored
442 daily from day 7 post-infection until parasites were detected. Clonality of the parasites in positive mice was
443 verified by integration PCR using primers listed in Tables 1, 2, and 3.

444 **Cell culture**

445 Human epithelial HeLa cells (European Cell Culture Collection) were maintained in Minimum Essential
446 Medium (MEM; 1-31F01-I BioConcept) supplemented with Earle's salts and 10% heat-inactivated fetal
447 bovine serum (FBS; Sigma-Aldrich), hereafter referred to as complete MEM (cMEM). Primary hepatocytes
448 were cultured in William's Medium E (WME) complete medium. All cells were incubated at 37°C under 5%
449 CO_2. For infection assays, 40,000 HeLa cells were seeded onto coverslips in 24-well plates and allowed to
450 adhere overnight. Cells were then infected with *P. berghei* sporozoites and maintained in cMEM containing
451 2.5 µg/mL amphotericin B (PAA Laboratories, P11-001) to prevent fungal contamination. Medium was
452 exchanged every 24 hours.

453 **Primary hepatocyte isolation**

454 The mice primary hepatocytes were isolated according to the method described (8). Briefly, the cells were
455 isolated from 12 to16 week old Balb/c or C57BL/6 mice using a two-step perfusion technique (8,83,102).
456 Mice were euthanized via CO_2 inhalation (1–2 minutes), and after securing the animal in a supine position,
457 a midline abdominal incision was made to expose the portal vein or inferior vena cava (IVC). A peristaltic
458 pump was pre-rinsed with 70% ethanol and HEPES buffer, then set to 50 for initial cannulation of the portal
459 vein (or IVC) using a Teflon-coated needle. Upon successful insertion, the flow was increased to maximum
460 (999), and the opposing vein was severed to allow perfusion with HEPES buffer for 5 minutes, during which
461 periodic clamping (10 seconds per minute) of the cut vein was performed. The tubing was subsequently
462 changed to a collagenase solution, and perfusion was held for 7 minutes with repeated clamping. The liver
463 was excised, transferred to a collagenase-containing well, and mechanically dissociated using filter tips and
464 gentle shaking with forceps. Cell suspensions were sequentially collected, pooled, and washed with

465 William's Medium E (WME) by centrifugation at 50g for 2 minutes. The pellet was resuspended in WME,
466 optionally passed through a 70 µm nylon strainer, and washed twice more. The final pellet was resuspended
467 in WME complete medium (WME supplemented with L-glutamine, penicillin-streptomycin, amphotericin B,
468 insulin-transferrin, and aprotinin), and cells were counted and seeded at densities appropriate for T25
469 flasks, GB dishes, or 24-well plates. After initial adhesion (1 hour), culture medium was supplemented or
470 exchanged after 2–4 hours.

471 **Immunofluorescence assay (IFA) of fixed primary hepatocytes and HeLa cells**

472 Immunofluorescence was carried out as previously described (56,86,103). Cells were seeded onto
473 coverslips in culture 24 well-plates and allowed to adhere overnight before infection. Infection was
474 maintained for 24 hours post-infection (hpi), after which cells were fixed using cold methanol at -20°C for
475 15 minutes and subsequently washed twice with Phosphate buffered saline (PBS). Blocking was performed
476 by incubating cells in 10% FCS in PBS for 20 minutes at room temperature to reduce non-specific binding.
477 Primary antibodies staining was carried out by incubating cells in 10% of FCS diluted in PBS for 1 hour at
478 room temperature, followed by three washes with PBS. Secondary antibodies incubation was performed in
479 10% of FCS as well for 1 hour at room temperature in the dark. The antibodies used are listed in the
480 enumerated session bellow. After three additional washes with PBS, nuclei were counterstained with DAPI.
481 Coverslips were then mounted onto slides with DAKO mounting medium and fluorescence imaging was
482 performed using either Nikon W1 or LIPSI and Crest V3 confocal microscope equipped with filters for DAPI
483 (4,6-Diamidin-2-phenylindol), AF488, AF594, and Cy5. Single-stain controls were carried out for every
484 staining to ensure that bleed-through was negligible.

485 **Sporozoite isolation from mosquito salivary glands and haemolymph**

486 *Anopheles mosquitoes* were fed on *Plasmodium*-infected mice exhibiting a gametocytaemia of 0.2 to 1%
487 and the sporozoite isolations were performed from day 18 post-infection as previously described (16,61).
488 For salivary gland sporozoites, mosquitoes were anesthetized with chloroform, sterilized in 70% ethanol,
489 and rinsed twice in PBS. The mosquitoes were then dissected, and salivary glands were extracted under a
490 binocular microscope in Iscove's Modified Dulbecco's Medium (IMDM) pooled in 50 µL of ice-cold IMDM
491 and mechanically homogenized using a pestle (Sigma-Aldrich, Z359947) powered with cordless motor
492 (Sigma-Aldrich, Z359971) as described (16,61). For hemolymph sporozoite extraction, glass capillaries
493 were heat-pulled to fine tips. The abdominal terminal segment of the mosquito was excised, and
494 hemolymph was flushed from the thorax by PBS perfusion via capillary insertion (75,104) . Hemolymphs
495 extracted were centrifuged (11,000 × g, 1 min), and pellets were resuspended in PBS or IMDM.
496 Sporozoite quantification was performed using a Neubauer hemacytometer. Midgut, hemolymph, or
497 salivary gland suspensions were mixed 1:1 with RPMI-1640 supplemented 10% FCS, and sporozoites
498 within four corner grids were counted. Total yields (sporozoites/mL and per mosquito) were calculated
499 based on dilution factors and dissection numbers.

500 **Sporozoites IFA and gliding motility assay**

501 To perform the sporozoite immunofluorescence assay (IFA), 12 mm cover glasses (0111530, Paul
502 Marienfeld, Germany) were coated with 0.1 mg/mL poly-D-lysine (A38904-01, Gibco, USA) (56,105) and
503 incubated overnight at room temperature. The following day, sporozoites were isolated from mosquito
504 midguts, hemolymph, or salivary glands as described above. The extracted sporozoites were suspended
505 in RPMI-1640 medium to a final volume of 200 µL in an Eppendorf tube and centrifuged at 1000 rpm for 3
506 min. The pellet was fixed by resuspension in 200 µL of cold methanol and incubated for 15 min at −20°C.
507 After fixation, sporozoites were washed twice with PBS (1000 rpm centrifugation) and transferred onto poly-
508 D-lysine-coated cover glasses in a 24-well plate (400024, Bioswisstec, Switzerland). The plate was

509 incubated for 30 min at room temperature to facilitate sporozoite adhesion before proceeding with either
510 the IFA or expansion microscopy protocol.
511 For the gliding motility assay, 5 µL of the sporozoite suspension in RPMI-1640 (supplemented with 10%
512 FCS) was added to 96-well glass-bottom plates (P96-1.5H-N, Cellvis, USA) (56,72,73). The plate was
513 centrifuged (1000 rpm, 1 min) and immediately live imaged using a Leica DM5500 widefield fluorescence
514 microscope.

515 **Expansion microscopy**

516 Expansion microscopy (PS-ExM) was performed as previously established (56–58). Infected cells (HeLa
517 cells, primary hepatocytes and sporozoites) were seeded on 13 mm coverslips in 24-well plates and fixed
518 with either 4% paraformaldehyde (PFA; F8775, Sigma) or cold methanol. The cells were anchored by
519 incubation in PBS containing 0.7% formaldehyde and 1% acrylamide at 37°C for 2 hours. Gelation was
520 then performed by adding 5 µL each of 10% tetramethylethylenediamine (TEMED; 17919, Thermo Fisher)
521 and 10% ammonium persulfate (APS) to 90 µL of monomer solution containing 19% sodium acrylate
522 (408220, Sigma), 10% acrylamide (A4058, Sigma), and 0.1% N, N'-methylenebisacrylamide (M1533,
523 Sigma). A 35 µL of monomer solution was dispensed onto parafilm in a humidity chamber, and coverslips
524 containing the anchored cells were inverted onto droplets. Following 5 minutes incubation on ice to improve
525 gel penetration, gels were polymerized at 37°C for 30 minutes. Gel-embedded samples were transferred
526 to denaturation buffer (200 mM SDS, 200 mM NaCl, 50 mM Tris-HCl, pH 9) in 6-well plates and agitated
527 (200 rpm) at room temperature for 15 minutes, followed by incubation in fresh buffer at 95°C for 1 hour with
528 gentle shaking. Gel expansion was performed in autoclaved MilliQ water (50 mL) for 1 hour with optional
529 buffer exchange. For immunostaining, gels were incubated with primary antibodies in 2% BSA for 2 hours
530 at 37°C, washed with PBS-Tween 0.1%, then labelled with secondary antibodies plus 1 µg/mL DAPI for
531 nuclear staining in 2% BSA for 2 hours at 37°C. Final gel expansion was conducted in MilliQ water
532 containing 0.2% propyl gallate (02370, Sigma) to prevent photobleaching. Expanded samples were
533 mounted on poly-D-lysine-coated (A38904, Gibco USA) glass-bottom dishes with cellular surfaces facing
534 downward and imaged with confocal microscopy.

535 **Antibodies used for IFA and expansion microscopy**

536 The primary antibodies used were: anti-UIS4 chicken (1:1000 IFA/1:500 expansion; Proteogenix), anti-UIS4
537 rabbit (1:1000 IFA/1:500 expansion; P. Sinnis, Baltimore), polyglutamylation IN105 rabbit (1:1000 IFA/1:500
538 expansion; AG-25B-0030-C050, AdipoGen Life Sciences), anti-GFP rabbit (1:1000 IFA/1:500 expansion;
539 SP3005P, Origene), anti-α-tubulin guinea pig (1:500 IFA/1:125 expansion; AA345, ABCD), anti-β-tubulin
540 guinea pig (1:500 IFA/1:125 expansion; AA344, ABCD), anti-tyrosinated tubulin mouse (1:1000 IFA/1:500
541 expansion; T9028, Sigma Aldrich), anti-polyglutamylation GT335 mouse (AG-20B-0020-C100, AdipoGen
542 Life Sciences), anti-γ-tubulin mouse (1:1000 IFA/1:500 expansion; T6557, Sigma Aldrich), and anti-GFP
543 mouse (1:1000 IFA/1:500 expansion; 814460001, Roche).
544 Secondary antibodies included anti-chicken IgY Alexa Fluor 594 (1:1000 IFA/1:500 expansion; A11042,
545 Invitrogen Molecular Probes), anti-rabbit IgG Alexa Fluor 594 (1:1000 IFA/1:500 expansion; A21207, Life
546 Technologies) and 488 (1:1000 IFA/1:500 expansion; A11034, Sigma Aldrich), anti-rabbit IgG ATTO 647N
547 (1:1000 expansion only; 40839, Sigma Aldrich), anti-guinea pig IgG Alexa Fluor 647 (1:1000 IFA/1:500
548 expansion; SAB4600033, Sigma Aldrich) and 594 (1:1000 IFA/1:500 expansion; A11076, Invitrogen
549 Molecular Probes), and anti-mouse IgG ATTO 647N (1:1000 expansion only; 50185, Sigma Aldrich) and
550 Alexa Fluor 488 (1:1000 IFA/1:500 expansion; A11001, Invitrogen Molecular Probes).

551 **In vivo assay**

To assess the infectivity of parasite mutant sporozoites to hepatocytes, *Anopheles stephensi* mosquitoes infected with different parasite mutants were allowed to feed on anesthetized naïve mice as previously described (Atchou et al., 2025). Three mice per parasite line and five mosquitoes per mouse were used. The blood stage infection progression was monitored daily via flow cytometry, starting from the day of infection until mice tested positive.

Oocyst size measurement

To quantify oocyst size, *Anopheles stephensi* mosquitoes were allowed to feed on anesthetized mice infected with the parasite (Rogerio et al. 2006; Hegge et al., 2009). At 7- and 11-days post-feeding, ten mosquitoes per time point were dissected, and their midguts were extracted and placed in 1× PBS. The midguts were then transferred to a 21-well microscopy slide, covered with a coverslip, and imaged using a Nikon Crest V3 confocal microscope (10× objective). The oocyst area was measured using Fiji software (ImageJ). Each experiment was performed in triplicate for every parasite line.

Liver stage parasite size measurement

To quantify the parasite size during liver stage development, HeLa cells (40,000 cells/well, triplicate) were seeded in 96-well plates and infected 24 hours later with 20,000 sporozoites per well. After a 2-hour incubation at 37°C, infected cells from each well were washed and redistributed into eight wells across two 96 well plates (4 wells/plate) to optimize cell density for imaging (Pino et al., 2017; Atchou et al., 2025; Sturm et al., 2006). Parasite development was analyzed at 6, 24, and 48 hpi using an InCell Analyzer 2000 with 10x objective. The image processing parameters such as kernel size, sensitivity, and size thresholds were optimized in InCell Developer software to distinguish individual parasites from background signals. Parasite growth was assessed based on size measurements, while survival rates were calculated as percentages relative to 6 hpi baseline counts.

Live cell imaging of *Plasmodium* microtubule dynamism

HeLa cells were seeded in a 96-well plate and infected the following day with *P. berghei* salivary gland sporozoites. After a 2-hour incubation at 37°C, cells were washed with MEM medium to remove uninfected parasites and residual mosquito salivary gland materials. The infected cells were then reseeded in a dark 24-well glass-bottom plate (Cellvis) and maintained in fresh cMEM at 37°C with 5% CO_2 (16,106). Prior to live imaging, cells were incubated for 1 hour in cMEM containing the SPY650-tubulin probe (1:1000 dilution; SC503, Spirochrome, Switzerland). Images were acquired using a Nikon W1 LIPSI spinning disk microscope with a 100X objective. Marked infected HeLa cells were imaged at defined time points to generate time-lapse movies capturing tubulin dynamics and parasite development.

Image processing and data analysis

All the live cell imaging, expansion microscopy, and IFA images in this study were acquired with Nikon W1 LIPSI and Crest V3, both in spinning disk mode. The microscope images were processed and analyzed using FIJI software, Huygens deconvolution Professional version (Huygens Remote Manager v3.8, Scientific Volume Imaging, The Netherlands), or, when specified, the 3D and 4D IMARIS software (Imaris 10.2.0; June 18, 2024). The 3D/4D image analysis software was used to segment the parasite LSPMB, hemi-spindle, and poles into either isospots or isosurfaces, as previously described (16,56). The counts, volumes, and coefficients of the isospots or isosurfaces were retrieved in .csv files, which were then imported into GraphPad Prism for statistical analysis. All data were analyzed using GraphPad Prism version 10.4.1 for macOS (GraphPad Software, San Diego, California, USA). Statistical comparisons were performed using one-way ANOVA with Dunn's multiple comparisons test (*$p \leq 0.05$, $p \leq 0.01$, *$p \leq 0.001$). All experiments in the study were carried out in triplicate.

Acknowledgments

The authors gratefully acknowledge the Microscopy Imaging Center (MIC) at the University of Bern, Switzerland, for their technical support and access to microscopy equipment. K.A. acknowledges the Swiss Confederation for the award of a Government Excellence Scholarship. *This work was funded by the Swiss National Science Foundation (SNSF) (grant number 310030_212795) and an Multidisciplinary Center for Infectious Diseases (MCID), University of Bern, Switzerland, grant to Volker Heussler (MA-09).*

References

1. Wambani J, Okoth P. Impact of Malaria Diagnostic Technologies on the Disease Burden in the Sub-Saharan Africa. 2022; Available from: https://onlinelibrary.wiley.com/doi/10.1155/2022/7324281

2. Poespoprodjo JR, Douglas NM, Ansong D, Kho S, Anstey NM. Malaria. Lancet [Internet]. 2023 Dec 16 [cited 2025 Mar 10];402(10419):2328–45. Available from: https://pubmed.ncbi.nlm.nih.gov/37924827/

3. Varo R, Chaccour C, Bassat Q. Update on malaria. Med Clin (Barc) [Internet]. 2020 Nov 13 [cited 2025 Mar 10];155(9):395–402. Available from: https://pubmed.ncbi.nlm.nih.gov/32620355/

4. Venkatesan P. WHO world malaria report 2024. Lancet Microbe [Internet]. 2025 Apr 1 [cited 2025 Jun 11];6(4):101073. Available from: https://www.thelancet.com/action/showFullText?pii=S2666524725000011

5. Tavares J, Formaglio P, Thiberge S, Mordelet E, Van Rooijen N, Medvinsky A, et al. Role of host cell traversal by the malaria sporozoite during liver infection. Journal of Experimental Medicine [Internet]. 2013 May 6 [cited 2025 May 18];210(5):905–15. Available from: www.jem.org/cgi/doi/10.1084/jem.20121130

6. Bindschedler A, Wacker R, Egli J, Eickel N, Schmuckli-Maurer J, Franke-Fayard BM, et al. Plasmodium berghei sporozoites in nonreplicative vacuole are eliminated by a PI3P-mediated autophagy-independent pathway. Cell Microbiol [Internet]. 2021 Jan 1 [cited 2025 Mar 10];23(1). Available from: https://pubmed.ncbi.nlm.nih.gov/32979009/

7. Marques-da-Silva C, Schmidt-Silva C, Kurup SP. Hepatocytes and the art of killing Plasmodium softly. Trends Parasitol [Internet]. 2024 Jun 1 [cited 2025 May 18];40(6):466–76. Available from: https://www.cell.com/action/showFullText?pii=S1471492224000862

8. Prado M, Eickel N, De Niz M, Heitmann A, Agop-Nersesian C, Wacker R, et al. Long-term live imaging reveals cytosolic immune responses of host hepatocytes against Plasmodium infection and parasite escape mechanisms. Autophagy [Internet]. 2015 [cited 2023 Jan 19];11(9):1561–79. Available from: https://pubmed.ncbi.nlm.nih.gov/26208778/

9. Zanghi G, Vaughan AM. Plasmodium vivax pre-erythrocytic stages and the latent hypnozoite. Parasitol Int. 2021 Dec 1;85:102447.

10. Prudêncio M, Rodriguez A, Mota MM. The silent path to thousands of merozoites: the Plasmodium liver stage. Nature Reviews Microbiology 2006 4:11 [Internet]. 2006 Nov [cited 2025 May 18];4(11):849–56. Available from: https://www.nature.com/articles/nrmicro1529

11. Roques M, Bindschedler A, Beyeler R, Heussler VT. Same, same but different: Exploring Plasmodium cell division during liver stage development. PLoS Pathog [Internet]. 2023 Mar 1 [cited 2025 Mar 12];19(3):e1011210. Available from: https://pmc.ncbi.nlm.nih.gov/articles/PMC10062574/

12. Shears MJ, Sekhar Nirujogi R, Swearingen KE, Renuse S, Mishra S, Jaipal Reddy P, et al. Proteomic Analysis of Plasmodium Merosomes: The Link between Liver and Blood Stages in Malaria. J Proteome Res [Internet]. 2019 Sep 6 [cited 2025 May 18];18(9):3404–18. Available from: https://pubs.acs.org/doi/full/10.1021/acs.jproteome.9b00324

13. De Niz M, Heussler VT. Rodent malaria models: insights into human disease and parasite biology. Curr Opin Microbiol [Internet]. 2018 Dec 1 [cited 2025 May 18];46:93–101. Available from: https://pubmed.ncbi.nlm.nih.gov/30317152/

14. Sturm A, Amino R, Van De Sand C, Regen T, Retzlaff S, Rennenberg A, et al. Manipulation of host hepatocytes by the malaria parasite for delivery into liver sinusoids. Science (1979) [Internet]. 2006 Sep 1 [cited 2024 May 16];313(5791):1287–90. Available from: https://www.science.org/doi/10.1126/science.1129720

15. Heussler V, Spielmann T, Frischknecht F, Gilberger T. Plasmodium. Molecular Parasitology: Protozoan Parasites and their Molecules [Internet]. 2016 Jan 1 [cited 2025 Mar 10];241–84. Available from: https://link.springer.com/chapter/10.1007/978-3-7091-1416-2_9

16. Atchou K, Caldelari R, Roques M, Schmuckli-Maurer J, Beyeler R, Heussler V. Expanding the fluorescent toolkit: Blue fluorescent protein-expressing Plasmodium berghei for enhanced multiplex microscopy. Portugaliza HP, editor. PLoS One [Internet]. 2025 Mar 3 [cited 2025 Mar 10];20(3):e0308055. Available from: https://pubmed.ncbi.nlm.nih.gov/40029851/

17. Stanway RR, Bushell E, Chiappino-Pepe A, Roques M, Sanderson T, Franke-Fayard B, et al. Genome-Scale Identification of Essential Metabolic Processes for Targeting the Plasmodium Liver Stage. Cell [Internet]. 2019 Nov 14 [cited 2025 Mar 10];179(5):1112-1128.e26. Available from: https://pubmed.ncbi.nlm.nih.gov/31730853/

18. Meibalan E, Marti M. Biology of Malaria Transmission. Cold Spring Harb Perspect Med [Internet]. 2017 Mar 1 [cited 2025 Mar 10];7(3). Available from: https://pubmed.ncbi.nlm.nih.gov/27836912/

19. Frischknecht F, Baldacci P, Martin B, Zimmer C, Thiberge S, Olivo-Marin JC, et al. Imaging movement of malaria parasites during transmission by Anopheles mosquitoes. Cell Microbiol [Internet]. 2004 Jul 1 [cited 2025 May 18];6(7):687–94. Available from: https://onlinelibrary.wiley.com/doi/full/10.1111/j.1462-5822.2004.00395.x

20. Vanderberg JP. Development of infectivity by the Plasmodium berghei sporozoite. Journal of Parasitology. 1975;61(1):43–50.

21. Vanderberg jerome P. Studies on the Motility of Plasmodium Sporozoites*. J Protozool [Internet]. 1974 Oct 1 [cited 2025 May 18];21(4):527–37. Available from: https://onlinelibrary.wiley.com/doi/full/10.1111/j.1550-7408.1974.tb03693.x

22. Frischknecht F, Matuschewski K. Plasmodium Sporozoite Biology. Cold Spring Harb Perspect Med [Internet]. 2017 May 1 [cited 2025 May 18];7(5):a025478. Available from: https://pmc.ncbi.nlm.nih.gov/articles/PMC5411682/

23. Mitchison T, Kirschner M. Dynamic instability of microtubule growth. Nature 1984 312:5991 [Internet]. 1984 [cited 2025 Mar 11];312(5991):237–42. Available from: https://www.nature.com/articles/312237a0

24. Janke C, Magiera MM. The tubulin code and its role in controlling microtubule properties and functions. Nat Rev Mol Cell Biol. 2020 Jun 1;21(6):307–26.

25. Nogales E. Structural insights into microtubule function. Annu Rev Biophys Biomol Struct [Internet]. 2001 Jun 1 [cited 2025 Mar 11];30(Volume 30, 2001):397–420. Available from: https://www.annualreviews.org/content/journals/10.1146/annurev.biophys.30.1.397

26. Roll-Mecak A. The Tubulin Code in Microtubule Dynamics and Information Encoding. Dev Cell. 2020 Jul 6;54(1):7–20.

27. Bodakuntla S, Jijumon AS, Villablanca C, Gonzalez-Billault C, Janke C. Microtubule-Associated Proteins: Structuring the Cytoskeleton. Trends Cell Biol. 2019 Oct 1;29(10):804–19.

28. Lee G. Non-motor microtubule-associated proteins. Curr Opin Cell Biol. 1993;5(1):88–91.

29. Peng N, Nakamura F. Microtubule-associated proteins and enzymes modifying tubulin. Cytoskeleton [Internet]. 2023 Mar 1 [cited 2025 Mar 11];80(3–4):60–76. Available from: https://onlinelibrary.wiley.com/doi/full/10.1002/cm.21748

30. Peng N, Nakamura F. Microtubule-associated proteins and enzymes modifying tubulin. Cytoskeleton (Hoboken) [Internet]. 2023 Mar 1 [cited 2025 Mar 11];80(3–4):60–76. Available from: https://pubmed.ncbi.nlm.nih.gov/36798013/

31. Fennell BJ, Al-shatr ZA, Bell A. Isotype expression, post-translational modification and stage-dependent production of tubulins in erythrocytic Plasmodium falciparum. Int J Parasitol. 2008 Apr 1;38(5):527–39.

32. Rawlings DJ, Fujioka H, Fried M, Keister DB, Aikawa M, Kaslow DC. α-Tubulin II is a male-specific protein in Plasmodium falciparum. Mol Biochem Parasitol. 1992 Dec 1;56(2):239–50.

33. Arregui C, Busciglio J, Caceres A, Barra HS. Tyrosinated and detyrosinated microtubules in axonal processes of cerebellar macroneurons grown in culture. J Neurosci Res [Internet]. 1991 [cited 2025 Mar 11];28(2):171–81. Available from: https://pubmed.ncbi.nlm.nih.gov/1674546/

34. Webster DR, Gundersen GG, Bulinski JC, Borisy GG. Differential turnover of tyrosinated and detyrosinated microtubules. Proc Natl Acad Sci U S A [Internet]. 1987 [cited 2025 Mar 11];84(24):9040–4. Available from: https://pubmed.ncbi.nlm.nih.gov/3321065/

35. Sanyal C, Pietsch N, Ramirez Rios S, Peris L, Carrier L, Moutin MJ. The detyrosination/re-tyrosination cycle of tubulin and its role and dysfunction in neurons and cardiomyocytes. Semin Cell Dev Biol [Internet]. 2023 Mar 15 [cited 2025 Mar 11];137:46–62. Available from: https://pubmed.ncbi.nlm.nih.gov/34924330/

36. Girão H, Macário-Monteiro J, Figueiredo AC, Silva E Sousa R, Doria E, Demidov V, et al. α-tubulin detyrosination fine-tunes kinetochore-microtubule attachments. Nat Commun [Internet]. 2024 Dec 1 [cited 2025 Mar 11];15(1):9720. Available from: https://pubmed.ncbi.nlm.nih.gov/39521805/

37. Gagnon C, White D, Cosson J, Huitorel P, Eddé B, Desbruyères E, et al. The polyglutamylated lateral chain of alpha-tubulin plays a key role in flagellar motility. J Cell Sci [Internet]. 1996 Jun 1 [cited 2025 Mar 11];109(6):1545–53. Available from: https://dx.doi.org/10.1242/jcs.109.6.1545

38. Edde B, Rossier J, Le Caer JP, Prome JC, Desbruyeres E, Gros F, et al. Polyglutamylated alpha-tubulin can enter the tyrosination/detyrosination cycle. Biochemistry [Internet]. 1992 Feb 1 [cited 2025 Mar 11];31(2):403–10. Available from: https://pubmed.ncbi.nlm.nih.gov/1370628/

39. Ruse CI, Chin HG, Pradhan S. Polyglutamylation: biology and analysis. Amino Acids [Internet]. 2022 Apr 1 [cited 2025 Mar 11];54(4):529–42. Available from: https://pubmed.ncbi.nlm.nih.gov/35357568/

40. Zheng P, Obara CJ, Szczesna E, Nixon-Abell J, Mahalingan KK, Roll-Mecak A, et al. ER proteins decipher the tubulin code to regulate organelle distribution. Nature [Internet]. 2022 Jan 6 [cited 2025 Mar 11];601(7891):132–8. Available from: https://pubmed.ncbi.nlm.nih.gov/34912111/

41. Neff NF, Thomas JH, Grisafi P, Botstein D. Isolation of the beta-tubulin gene from yeast and demonstration of its essential function in vivo. Cell [Internet]. 1983 [cited 2025 Mar 11];33(1):211–9. Available from: https://pubmed.ncbi.nlm.nih.gov/6380751/

42. Baum P, Thorner J, Honig L. Identification of tubulin from the yeast Saccharomyces cerevisiae. Proc Natl Acad Sci U S A. 1978;75(10):4962–6.

43. Hirst WG, Fachet D, Kuropka B, Weise C, Saliba KJ, Reber S. Purification of functional Plasmodium falciparum tubulin allows for the identification of parasite-specific microtubule inhibitors. Current Biology. 2022 Feb 28;32(4):919-926.e6.

44. Holloway SP, Gerousis M, Delves CJ, Sims PFG, Scaife JG, Hyde JE. The tubulin genes of the human malaria parasite Plasmodium falciparum, their chromosomal location and sequence analysis of the α-tubulin II gene. Mol Biochem Parasitol. 1990 Dec 1;43(2):257–70.

45. Fennell BJ, Naughton JA, Dempsey E, Bell A. Cellular and molecular actions of dinitroaniline and phosphorothioamidate herbicides on Plasmodium falciparum: tubulin as a specific antimalarial target. Mol Biochem Parasitol [Internet]. 2006 Feb [cited 2025 Mar 11];145(2):226–38. Available from: https://pubmed.ncbi.nlm.nih.gov/16406111/

46. Dow GS, Armson A, Boddy MR, Itenge T, McCarthy D, Parkin JE, et al. Plasmodium: assessment of the antimalarial potential of trifluralin and related compounds using a rat model of malaria, Rattus norvegicus. Exp Parasitol [Internet]. 2002 Mar 1 [cited 2025 Mar 11];100(3):155–60. Available from: https://pubmed.ncbi.nlm.nih.gov/12173400/

47. Dempsey E, Prudêncio M, Fennell BJ, Gomes-Santos CS, Barlow JW, Bell A. Antimitotic herbicides bind to an unidentified site on malarial parasite tubulin and block development of liver-stage Plasmodium parasites. Mol Biochem Parasitol [Internet]. 2013 Apr [cited 2025 Mar 11];188(2):116–27. Available from: https://pubmed.ncbi.nlm.nih.gov/23523992/

48. Kooij TWA, Franke-Fayard B, Renz J, Kroeze H, Van Dooren MW, Ramesar J, et al. Plasmodium berghei alpha-tubulin II: a role in both male gamete formation and asexual blood stages. Mol Biochem Parasitol [Internet]. 2005 Nov [cited 2025 Mar 11];144(1):16–26. Available from: https://pubmed.ncbi.nlm.nih.gov/16115694/

49. Holloway SP, Sims PFG, Delves CJ, Scaife JG, Hyde JE. Isolation of alpha-tubulin genes from the human malaria parasite, Plasmodium falciparum: sequence analysis of alpha-tubulin. Mol Microbiol [Internet]. 1989 [cited 2025 Mar 11];3(11):1501–10. Available from: https://pubmed.ncbi.nlm.nih.gov/2693901/

50. Spreng B, Fleckenstein H, Kübler P, Di Biagio C, Benz M, Patra P, et al. Microtubule number and length determine cellular shape and function in Plasmodium . EMBO J [Internet]. 2019 Aug 24 [cited 2025 Mar 11];38(15). Available from: https://www.embopress.org/doi/10.15252/embj.2018100984

51. Zhang G, Niu G, Hooker–Romera D, Shabani S, Ramelow J, Wang X, et al. Targeting plasmodium α-tubulin-1 to block malaria transmission to mosquitoes. Front Cell Infect Microbiol [Internet]. 2023 [cited 2025 Mar 11];13:1132647. Available from: https://pmc.ncbi.nlm.nih.gov/articles/PMC10064449/

52. Valenstein ML, Roll-Mecak A. Graded Control of Microtubule Severing by Tubulin Glutamylation. Cell [Internet]. 2016 Feb 25 [cited 2025 Mar 11];164(5):911–21. Available from: https://www.cell.com/action/showFullText?pii=S0092867416000593

53. Bonnet C, Boucher D, Lazereg S, Pedrotti B, Islam K, Denoulet P, et al. Differential Binding Regulation of Microtubule-associated Proteins MAP1A, MAP1B, and MAP2 by Tubulin Polyglutamylation. Journal of Biological Chemistry [Internet]. 2001 Apr 20 [cited 2025 Mar 11];276(16):12839–48. Available from: https://www.jbc.org/action/showFullText?pii=S0021925819343935

54. Bertiaux E, Balestra AC, Bournonville L, Louvel V, Maco B, Soldati-Favre D, et al. Expansion microscopy provides new insights into the cytoskeleton of malaria parasites including the conservation of a conoid. PLoS Biol [Internet]. 2021 Mar 11 [cited 2025 Mar 11];19(3). Available from: https://pubmed.ncbi.nlm.nih.gov/33705377/

55. Hentzschel F, Binder AM, Dorner LP, Herzel L, Nuglisch F, Sema M, et al. Microtubule inner proteins of Plasmodium are essential for transmission of malaria parasites. Proceedings of the National Academy of Sciences [Internet]. 2025 Feb 11 [cited 2025 Mar 12];122(6):e2421737122. Available from: https://www.pnas.org/doi/abs/10.1073/pnas.2421737122

56. Atchou K, Berger BM, Heussler V, Ochsenreiter T. Pre-gelation staining expansion microscopy for visualisation of the Plasmodium liver stage. J Cell Sci [Internet]. 2023 [cited 2025 Mar 11];136(22):jcs261377. Available from: https://pmc.ncbi.nlm.nih.gov/articles/PMC10729816/

57. Liffner B, Absalon S. Expansion microscopy of apicomplexan parasites. Mol Microbiol [Internet]. 2024 Apr 1 [cited 2025 Mar 11];121(4):619–35. Available from: https://pubmed.ncbi.nlm.nih.gov/37571814/

58. Liffner B, Diaz AKC, Blauwkamp J, Anaguano D, Frolich S, Muralidharan V, et al. Atlas of Plasmodium falciparum intraerythrocytic development using expansion microscopy. Elife [Internet]. 2023 Dec 18 [cited 2025 Mar 11];12. Available from: https://pubmed.ncbi.nlm.nih.gov/38108809/

59. Ferreira JL, Pražák V, Vasishtan D, Siggel M, Hentzschel F, Binder AM, et al. Variable microtubule architecture in the malaria parasite. Nat Commun [Internet]. 2023 Dec 1 [cited 2025 Mar 12];14(1):1216. Available from: https://pmc.ncbi.nlm.nih.gov/articles/PMC9984467/

60. Aguayo-Ortiz R, Dominguez L. Unveiling the Possible Oryzalin-Binding Site in the α-Tubulin of Toxoplasma gondii. ACS Omega [Internet]. 2022 Jun 7 [cited 2025 Mar 12];7(22):18434–42. Available from: https://pubs.acs.org/doi/full/10.1021/acsomega.2c00729

61. Beyeler R, Jordan M, Dorner L, He B, Cyrklaff M, Roques M, et al. Putative prefoldin complex subunit 5 of Plasmodium berghei is crucial for microtubule formation and parasite development in the mosquito. Mol Microbiol [Internet]. 2024 Mar 1 [cited 2025 Mar 12];121(3):481–96. Available from: https://pubmed.ncbi.nlm.nih.gov/38009402/

62. Roques M, Stanway RR, Rea EI, Markus R, Brady D, Holder AA, et al. Plasmodium centrin PbCEN-4 localizes to the putative MTOC and is dispensable for malaria parasite proliferation. Biol Open [Internet]. 2019 Jan 1 [cited 2025 Mar 12];8(1):bio036822. Available from: https://pmc.ncbi.nlm.nih.gov/articles/PMC6361220/

63. Zeeshan M, Shilliday F, Liu T, Abel S, Mourier T, Ferguson DJP, et al. Plasmodium kinesin-8X associates with mitotic spindles and is essential for oocyst development during parasite proliferation and transmission. PLoS Pathog [Internet]. 2019 [cited 2025 Mar 12];15(10):e1008048. Available from: https://pmc.ncbi.nlm.nih.gov/articles/PMC6786531/

64. Yang S, Cai M, Huang J, Zhang S, Mo X, Jiang K, et al. EB1 decoration of microtubule lattice facilitates spindle-kinetochore lateral attachment in Plasmodium male gametogenesis. Nature Communications 2023 14:1 [Internet]. 2023 May 19 [cited 2025 Mar 12];14(1):1–20. Available from: https://www.nature.com/articles/s41467-023-38516-3

65. Mauer S, Camargo N, Abatiyow BA, Gargaro OR, Kappe SHI, Kumar S. Plasmodium microtubule-binding protein EB1 is critical for partitioning of nuclei in male gametogenesis. mBio [Internet]. 2023 Aug 31 [cited 2025 Mar 12];14(4):e00822-23. Available from: https://pmc.ncbi.nlm.nih.gov/articles/PMC10470552/

66. Magiera MM, Janke C. Investigating Tubulin Posttranslational Modifications with Specific Antibodies. Methods Cell Biol. 2013 Jan 1;115:247–67.

67. Oakley BR. gamma-Tubulin. Curr Top Dev Biol [Internet]. 2000 [cited 2025 Mar 11];49:27–54. Available from: https://pubmed.ncbi.nlm.nih.gov/11005013/

68. Maessen S, Wesseling JG, Smits MA, Konings RNH, Schoenmakers JGG. The γ-tubulin gene of the malaria parasite Plasmodium falciparum. Mol Biochem Parasitol. 1993 Jul 1;60(1):27–35.

69. Haase R, Puthenpurackal A, Maco B, Guérin A, Soldati-Favre D. γ-tubulin complex controls the nucleation of tubulin-based structures in Apicomplexa. Mol Biol Cell [Internet]. 2024 Sep 1 [cited 2025 Jun 21];35(9):ar121. Available from: https://pmc.ncbi.nlm.nih.gov/articles/PMC11449391/

70. Barik S, Andrews J. Host–Parasite Interactions in Toxoplasma gondii-Infected Cells: Roles of Mitochondria, Microtubules, and the Parasitophorous Vacuole. Int J Mol Sci [Internet]. 2024 Dec 1 [cited 2025 Jun 21];25(24):13459. Available from: https://pmc.ncbi.nlm.nih.gov/articles/PMC11677533/

71. Burda PC, Caldelari R, Heussler VT. Manipulation of the Host Cell Membrane during Plasmodium Liver Stage Egress. mBio [Internet]. 2017 Mar 1 [cited 2025 Mar 13];8(2). Available from: https://pubmed.ncbi.nlm.nih.gov/28400525/

72. Hopp CS, Chiou K, Ragheb DRT, Salman AM, Khan SM, Liu AJ, et al. Longitudinal analysis of plasmodium sporozoite motility in the dermis reveals component of blood vessel recognition. Elife. 2015 Aug 13;4(AUGUST2015).

73. Beyer K, Kracht S, Kehrer J, Singer M, Klug D, Frischknecht F. Limited Plasmodium sporozoite gliding motility in the absence of TRAP family adhesins. Malar J [Internet]. 2021 Dec 1 [cited 2023 Apr 12];20(1):1–12. Available from: https://malariajournal.biomedcentral.com/articles/10.1186/s12936-021-03960-3

74. Klug D, Frischknecht F. Motility precedes egress of malaria parasites from oocysts. Elife. 2017 Jan 24;6.

75. Braumann F, Klug D, Kehrer J, Song G, Feng J, Springer TA, et al. Conformational change of Plasmodium TRAP is essential for sporozoite migration and transmission . EMBO Rep [Internet]. 2023 Jul 5 [cited 2025 May 13];24(7). Available from: https://www.embopress.org/doi/10.15252/embr.202357064

76. Douglas RG, Reinig M, Neale M, Frischknecht F. Screening for potential prophylactics targeting sporozoite motility through the skin. Malar J [Internet]. 2018 Aug 31 [cited 2025 May 13];17(1). Available from: https://pubmed.ncbi.nlm.nih.gov/30170589/

77. Meis JFGM, Verhave JP, Jap PHK, Meuwissen JHET. Transformation of sporozoites of Plasmodium berghei into exoerythrocytic forms in the liver of its mammalian host. Cell Tissue Res [Internet]. 1985 Aug [cited 2025 Mar 13];241(2):353–60. Available from: https://link.springer.com/article/10.1007/BF00217180

78. Short B. Polyglutamylation makes the cut. J Cell Biol [Internet]. 2010 Jun 14 [cited 2025 Mar 12];189(6):920. Available from: https://pmc.ncbi.nlm.nih.gov/articles/PMC2886350/

79. Genova M, Grycova L, Puttrich V, Magiera MM, Lansky Z, Janke C, et al. Tubulin polyglutamylation differentially regulates microtubule-interacting proteins. EMBO J [Internet]. 2023 Mar [cited 2025 Mar 12];42(5):e112101. Available from: https://pmc.ncbi.nlm.nih.gov/articles/PMC9975938/

80. Pathak NH, Drummond IA. Polyglutamylation and the fleer gene. Methods Cell Biol. 2009;94:317–32.

81. Jayabalasingham B, Bano N, Coppens I. Metamorphosis of the malaria parasite in the liver is associated with organelle clearance. Cell Res [Internet]. 2010 Sep [cited 2025 Mar 12];20(9):1043. Available from: https://pmc.ncbi.nlm.nih.gov/articles/PMC4137911/

82. Graewe S, Stanway RR, Rennenberg A, Heussler VT. Chronicle of a death foretold: Plasmodium liver stage parasites decide on the fate of the host cell. FEMS Microbiol Rev [Internet]. 2012 Jan 1 [cited 2025 Mar 12];36(1):111–30. Available from: https://dx.doi.org/10.1111/j.1574-6976.2011.00297.x

83. de Niz M, Caldelari R, Kaiser G, Zuber B, Heo W Do, Heussler VT, et al. Hijacking of the host cell Golgi by Plasmodium berghei liver stage parasites. J Cell Sci [Internet]. 2021 May 1

879 [cited 2025 Mar 12];134(10):jcs252213. Available from:
880 https://pmc.ncbi.nlm.nih.gov/articles/PMC8186485/

881 84. O'neal AJ, Butler LR, Rolandelli A, Gilk SD, Pedra JHF. Lipid hijacking: A unifying theme in
882 vector-borne diseases. Elife. 2020 Oct 1;9:1–31.

883 85. Fraser M, Curtis B, Phillips P, Yates PA, Lam KS, Netzel O, et al. Harnessing cholesterol
884 uptake of malaria parasites for therapeutic applications. EMBO Mol Med [Internet]. 2024 Jul
885 15 [cited 2025 Mar 12];16(7):1515–32. Available from:
886 https://www.embopress.org/doi/10.1038/s44321-024-00087-1

887 86. Schmuckli-Maurer J, Bindschedler AF, Wacker R, Würgler OM, Rehmann R, Lehmberg T, et
888 al. Plasmodium berghei liver stage parasites exploit host GABARAP proteins for TFEB
889 activation. Communications Biology 2024 7:1 [Internet]. 2024 Nov 21 [cited 2025 Mar
890 12];7(1):1–13. Available from: https://www.nature.com/articles/s42003-024-07242-x

891 87. Zeeshan M, Rea E, Abel S, Vukušić K, Markus R, Brady D, et al. Plasmodium ARK2 and
892 EB1 drive unconventional spindle dynamics, during chromosome segregation in sexual
893 transmission stages. Nature Communications 2023 14:1 [Internet]. 2023 Sep 13 [cited 2025
894 Mar 12];14(1):1–19. Available from: https://www.nature.com/articles/s41467-023-41395-3

895 88. Van Dijk J, Miro J, Strub JM, Lacroix B, Van Dorsselaer A, Edde B, et al. Polyglutamylation Is
896 a Post-translational Modification with a Broad Range of Substrates. Journal of Biological
897 Chemistry. 2008 Feb 15;283(7):3915–22.

898 89. Morrissette N, Abbaali I, Ramakrishnan C, Hehl AB. The Tubulin Superfamily in
899 Apicomplexan Parasites. Microorganisms [Internet]. 2023 Mar 1 [cited 2025 Mar 11];11(3).
900 Available from: https://pubmed.ncbi.nlm.nih.gov/36985278/

901 90. Kappe SHI, Kaiser K, Matuschewski K. The Plasmodium sporozoite journey: a rite of
902 passage. Trends Parasitol. 2003 Mar 1;19(3):135–43.

903 91. Ferreira JL, Heincke D, Wichers JS, Liffner B, Wilson DW, Gilberger TW. The Dynamic Roles
904 of the Inner Membrane Complex in the Multiple Stages of the Malaria Parasite. Front Cell
905 Infect Microbiol. 2021 Jan 8;10:611801.

906 92. Harding CR, Meissner M. The inner membrane complex through development of Toxoplasma
907 gondii and Plasmodium. Cell Microbiol [Internet]. 2014 [cited 2025 Mar 13];16(5):632.
908 Available from: https://pmc.ncbi.nlm.nih.gov/articles/PMC4286798/

909 93. Burda PC, Roelli MA, Schaffner M, Khan SM, Janse CJ, Heussler VT. A Plasmodium
910 Phospholipase Is Involved in Disruption of the Liver Stage Parasitophorous Vacuole
911 Membrane. PLoS Pathog [Internet]. 2015 Mar 1 [cited 2025 Mar 13];11(3):e1004760.
912 Available from: https://pmc.ncbi.nlm.nih.gov/articles/PMC4364735/

913 94. Kaiser G, De Niz M, Zuber B, Burda PC, Kornmann B, Heussler VT, et al. High resolution
914 microscopy reveals an unusual architecture of the Plasmodium berghei endoplasmic
915 reticulum. Mol Microbiol [Internet]. 2016 Dec 1 [cited 2025 Mar 13];102(5):775–91. Available
916 from: https://pubmed.ncbi.nlm.nih.gov/27566438/

917 95. Philip N, Waters AP. Conditional degradation of plasmodium calcineurin reveals functions in
918 parasite colonization of both host and vector. Cell Host Microbe [Internet]. 2015 Jul 8 [cited

2025 Jun 21];18(1):122–31. Available from: https://www.cell.com/action/showFullText?pii=S1931312815002504

96. Lin J wen, Annoura T, Sajid M, Chevalley-Maurel S, Ramesar J, Klop O, et al. A novel “Gene Insertion/Marker Out” (GIMO) method for transgene expression and gene complementation in rodent malaria parasites. PLoS One. 2011 Dec 27;6(12).

97. Janse CJ, Ramesar J, Waters AP. High-efficiency transfection and drug selection of genetically transformed blood stages of the rodent malaria parasite Plasmodium berghei. Nature Protocols 2006 1:1 [Internet]. 2006 Jun 29 [cited 2025 Jun 21];1(1):346–56. Available from: https://www.nature.com/articles/nprot.2006.53

98. De Niz M, Stanway RR, Wacker R, Keller D, Heussler VT. An ultrasensitive NanoLuc-based luminescence system for monitoring Plasmodium berghei throughout its life cycle. Malaria Journal 2016 15:1 [Internet]. 2016 Apr 21 [cited 2025 Jun 20];15(1):1–24. Available from: https://malariajournal.biomedcentral.com/articles/10.1186/s12936-016-1291-9

99. Salman AM, Mogollon CM, Lin JW, Van Pul FJA, Janse CJ, Khan SM. Generation of transgenic rodent malaria parasites expressing human malaria parasite proteins. Methods in Molecular Biology. 2015;1325:257–86.

100. Govindarajalu G, Rizvi Z, Kumar D, Sijwali PS. Lyse-Reseal Erythrocytes for Transfection of Plasmodium falciparum. Sci Rep [Internet]. 2019 Dec 1 [cited 2024 Jan 23];9(1). Available from: /pmc/articles/PMC6934678/

101. Pino P, Caldelari R, Mukherjee B, Vahokoski J, Klages N, Maco B, et al. A multistage antimalarial targets the plasmepsins IX and X essential for invasion and egress. Science (1979) [Internet]. 2017 Oct 27 [cited 2025 Jun 20];358(6362):522–8. Available from: https://www.science.org/doi/10.1126/science.aaf8675

102. Kaur I, Vasudevan A, Rawal P, Tripathi DM, Ramakrishna S, Kaur S, et al. Primary Hepatocyte Isolation and Cultures: Technical Aspects, Challenges and Advancements. Bioengineering [Internet]. 2023 Feb 1 [cited 2025 Apr 25];10(2):131. Available from: https://pmc.ncbi.nlm.nih.gov/articles/PMC9952008/

103. Bindschedler A, Schmuckli-Maurer J, Buchser S, Fischer TD, Wacker R, Davalan T, et al. LC3B labeling of the parasitophorous vacuole membrane of Plasmodium berghei liver stage parasites depends on the V-ATPase and ATG16L1. Mol Microbiol [Internet]. 2024 Jun 1 [cited 2024 Nov 13];121(6):1095–111. Available from: https://onlinelibrary.wiley.com/doi/full/10.1111/mmi.15259

104. Blight J, Sala KA, Atcheson E, Kramer H, Turabi A El, Real E, et al. Dissection-independent production of Plasmodium sporozoites from whole mosquitoes. Life Sci Alliance [Internet]. 2021 Jul 1 [cited 2025 Apr 25];4(7):e202101094. Available from: https://pmc.ncbi.nlm.nih.gov/articles/PMC8321652/

105. Liffner B, Silva TLA e, Vega-Rodriguez J, Absalon S. Mosquito Tissue Ultrastructure-Expansion Microscopy (MoTissU-ExM) enables ultrastructural and anatomical analysis of malaria parasites and their mosquito. BMC Methods 2024 1:1 [Internet]. 2024 Oct 7 [cited 2025 Apr 25];1(1):1–15. Available from: https://bmcmethods.biomedcentral.com/articles/10.1186/s44330-024-00013-4

106. Rankin KE, Graewe S, Heussler VT, Stanway RR. Imaging liver-stage malaria parasites. Cell Microbiol [Internet]. 2010 May [cited 2023 Jan 19];12(5):569–79. Available from: https://pubmed.ncbi.nlm.nih.gov/20180802/

Figures

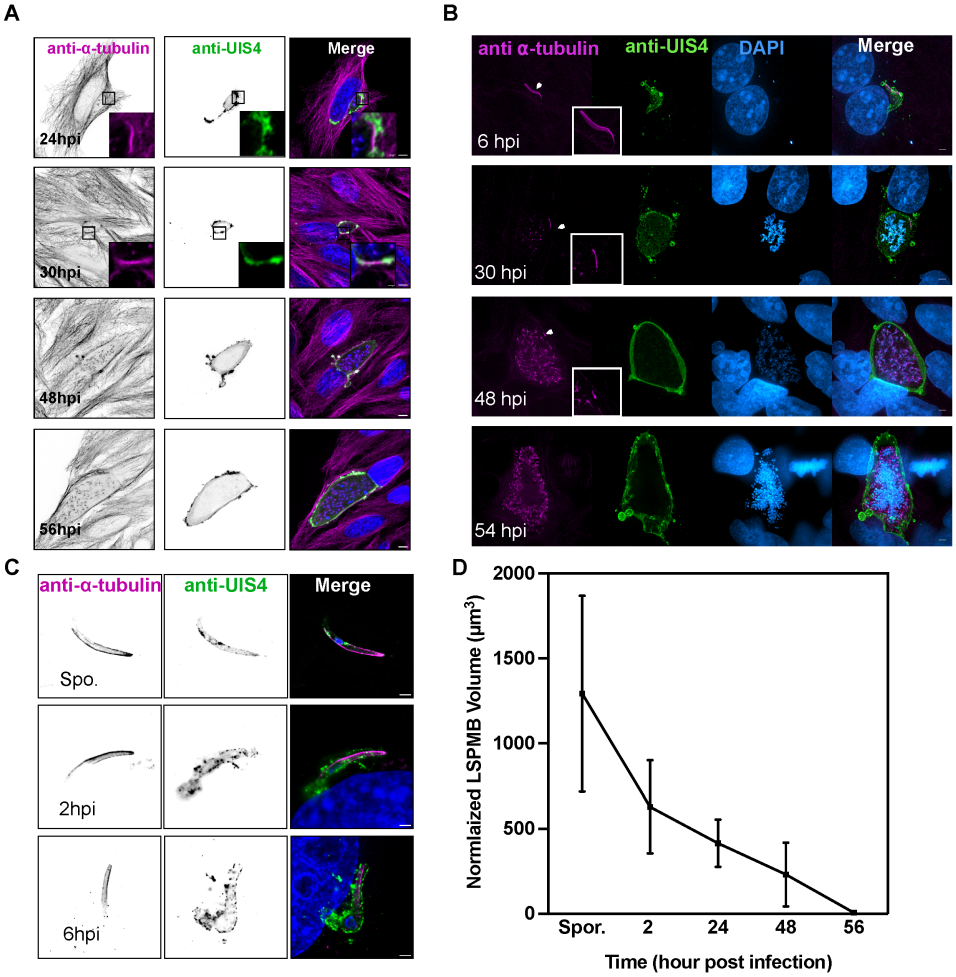
A
anti-α-tubulin
anti-UIS4
Merge
24hpi
30hpi
48hpi
56hpi
B
anti α-tubulin
anti-UIS4
DAPI
Merge
6 hpi
30 hpi
48 hpi
54 hpi
C
anti-α-tubulin
anti-UIS4
Merge
Spo.
2hpi
6hpi
D
Normlaized LSPMB Volume (μm³)
2000
1500
1000
500
0
Spor.
2
24
48
56
Time (hour post infection)

E

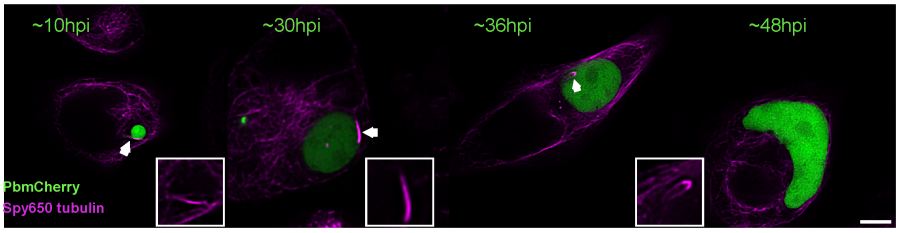
~10hpi
~30hpi
~36hpi
~48hpi
PbmCherry
Spy650 tubulin

966 **Figure 1:** Immunofluorescence assay and expansion microscopy (PS-ExM) reveals liver stage
967 parasite subpellicular microtubule. **(A)**, and **(B)**, show maximum projection of z-stacks confocal
968 images of infected HeLa cells and **(C)** sporozoites. Host and parasite microtubules were stained with
969 anti-α-tubulin (magenta), and nuclei with DAPI (blue). The parasitophorous membrane vacuole (PVM)
970 was stained with anti-UIS4 (green). **(A)** HeLa cells were infected with *Plasmodium* salivary glands
971 sporozoites and methanol-fixed at 24, 30, 48, and 56 hpi. IFA was performed. **(B)** Fixed infected HeLa
972 cells were expanded using the PS-ExM protocol. Inlets show LSPMB structures at 6, 30, and 48 hpi.
973 Scale bar: 10 µm. **(C)** To determine whether the LSPMB originates from the sporozoite stage, PS-
974 ExM was performed on salivary gland sporozoites, and parasite liver stage at 2 and 6 hpi. **(D)** LSPMB
975 volume was quantified from PS-ExM z-stacks using 3D and 4D analysis in IMARIS software.
976 Normalised mean volumes were: 1294.12 μm^3 in sporozoites, 628.34 μm^3 at 2 hpi, 414.84 μm^3 at 24
977 hpi, 231.4 μm^3 at 48 hpi, to 5.6 μm^3 at 54 hpi. **(E)** Live cell confocal imaging of infected HeLa cells
978 incubated with tubulin tracker SPY650. Images show microtubules at 10, 30, 36, and 48 hpi. Host and
979 parasite microtubules are shown in magenta; the parasite expresses cytosolic GFP (green). *Scale*
980 *bar: 5 µm.*

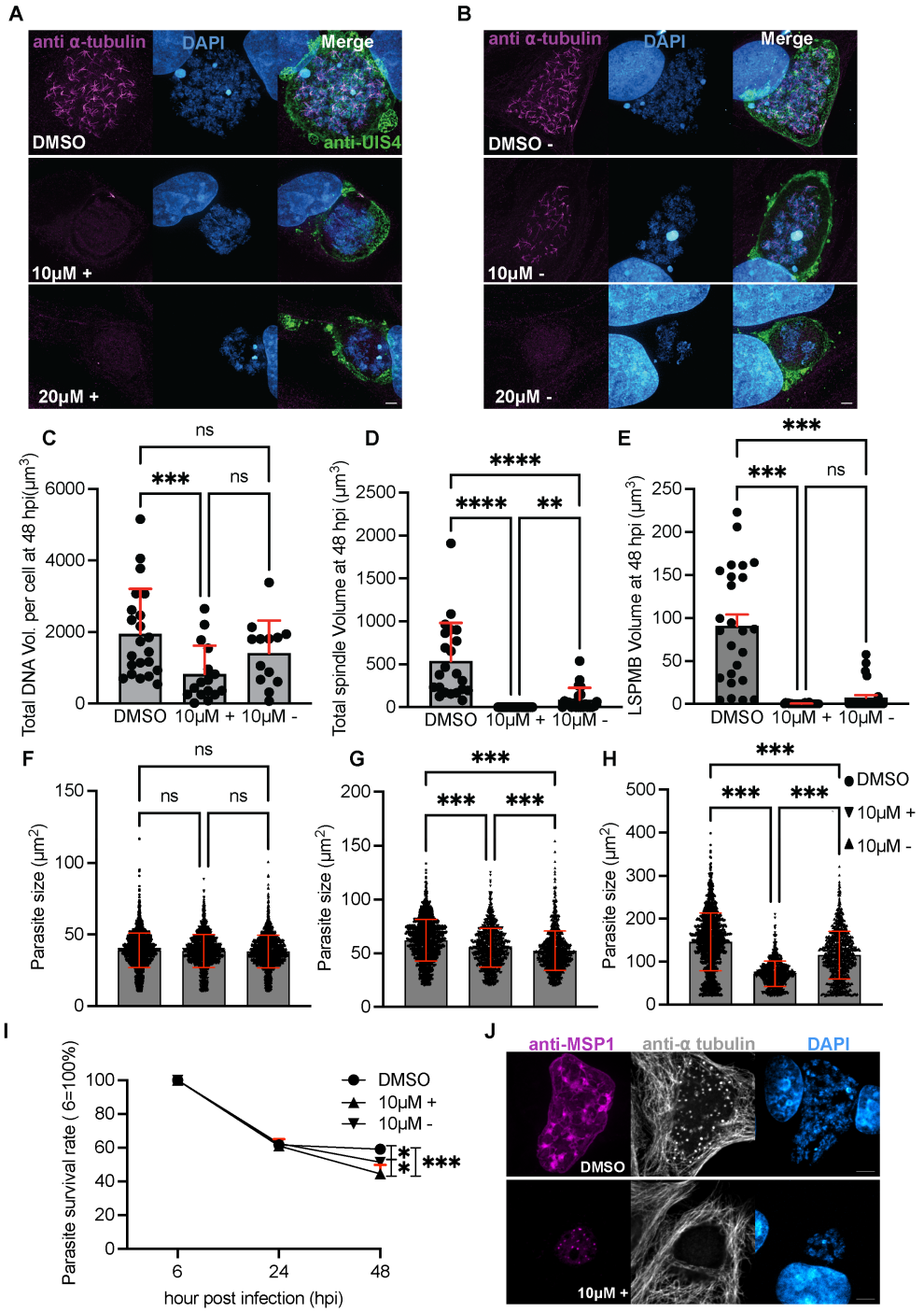
A
anti α-tubulin
DAPI
Merge
DMSO
anti-UIS4
10μM +
20μM +
B
anti α-tubulin
DAPI
Merge
DMSO -
10μM -
20μM -
C
Total DNA Vol. per cell at 48 hpi(μm3)
ns
***
ns
DMSO
10μM +
10μM -
D
Total spindle Volume at 48 hpi (μm3)
****
****
**
E
LSPMB Volume at 48 hpi (μm3)
***
***
ns
F
Parasite size (μm2)
ns
ns
ns
G
Parasite size (μm2)
***
***
***
H
Parasite size (μm2)
***
***
***
DMSO
10μM +
10μM -
I
Parasite survival rate (6=100%)
hour post infection (hpi)
DMSO
10μM +
10μM -
*
*
***
J
anti-MSP1
anti-α tubulin
DAPI
DMSO
10μM +

982 **Figure 2:** Microtubules are essential for *Plasmodium* liver stage development.
983 **(A** and **B)** show the effect of oryzalin on parasite microtubules during liver stage development.
984 Sporozoites isolated from mosquito salivary glands were incubated in medium containing either 10 or
985 20 µM of oryzalin. HeLa cells were infected and fixed at 48 hpi with cold methanol prior to PS-ExM.
986 **(A)** confocal z-stack projections of control cells (DMSO) and cells treated with 10 and 20 µM of
987 Oryzalin. **(B)** confocal z-stack projections of infected cells where oryzalin was washed out at 24 hpi.
988 Microtubule was stained with anti-α-tubulin (magenta), the PVM with anti UIS4 (green), and nuclei
989 with DAPI (blue). Scale bar: 10 µm. ''+'' indicates cells treated with Oryzalin; '' - '' indicates cells from
990 which the drug has been removed at 24 hpi. **(C)** Normalized total parasite DNA volume at 48 hpi.
991 Mean DNA volume was 1952.02 μm^3 in the DMSO control, 827.26 μm^3 in 10 µM oryzalin-treated cells,
992 and 1411.73 μm^3 after drug removal. **(D)** Normalized total hemi-spindle volume. The mean volume
993 was 539.3 μm^3 in the control, 0 μm^3 with oryzalin treatment, and 89.08 μm^3 after drug removal. **(E)**
994 Normalized LSPMB volume at 48 hpi. Mean volume was 5.92 μm^3 in the control, 2.3 μm^3 with oryzalin,
995 and 1.65 μm^3 after drug removal. **(F, G and H)** Parasite size measurement at 6, 24, and 48 hpi,
996 respectively. At 24 and 48 hpi, mean parasite size was 145.9 μm^2 in the control, 71.75 μm^2 with
997 oryzalin, and 115.3 μm^2 after drug removal. **(I)** Parasite survival rate from 6 to 48 hpi. A slight increase
998 in parasite death was observed in oryzalin-treated cells compared to the DMSO control. The red line
999 on the graphs represents the mean and standard deviation. **(C**, **D**, **E**, **F**, and **G)**, and **(H)**: each dot
1000 represents an individual quantified parasite. **(J)** Confocal z-stack projection of IFA images at 56 hpi in
1001 cells treated with 10 µM oryzalin and DMSO control. Cells were fixed with cold methanol and stained
1002 for MSP1 (magenta), α-tubulin (grey) and nuclei (DAPI, blue). Scale bar: 5 µm. Statistical comparisons
1003 were performed using one-way ANOVA with Dunnett's multiple comparisons test (*$p \leq 0.05$, **$p \leq$
1004 0.01, ***$p \leq 0.001$).

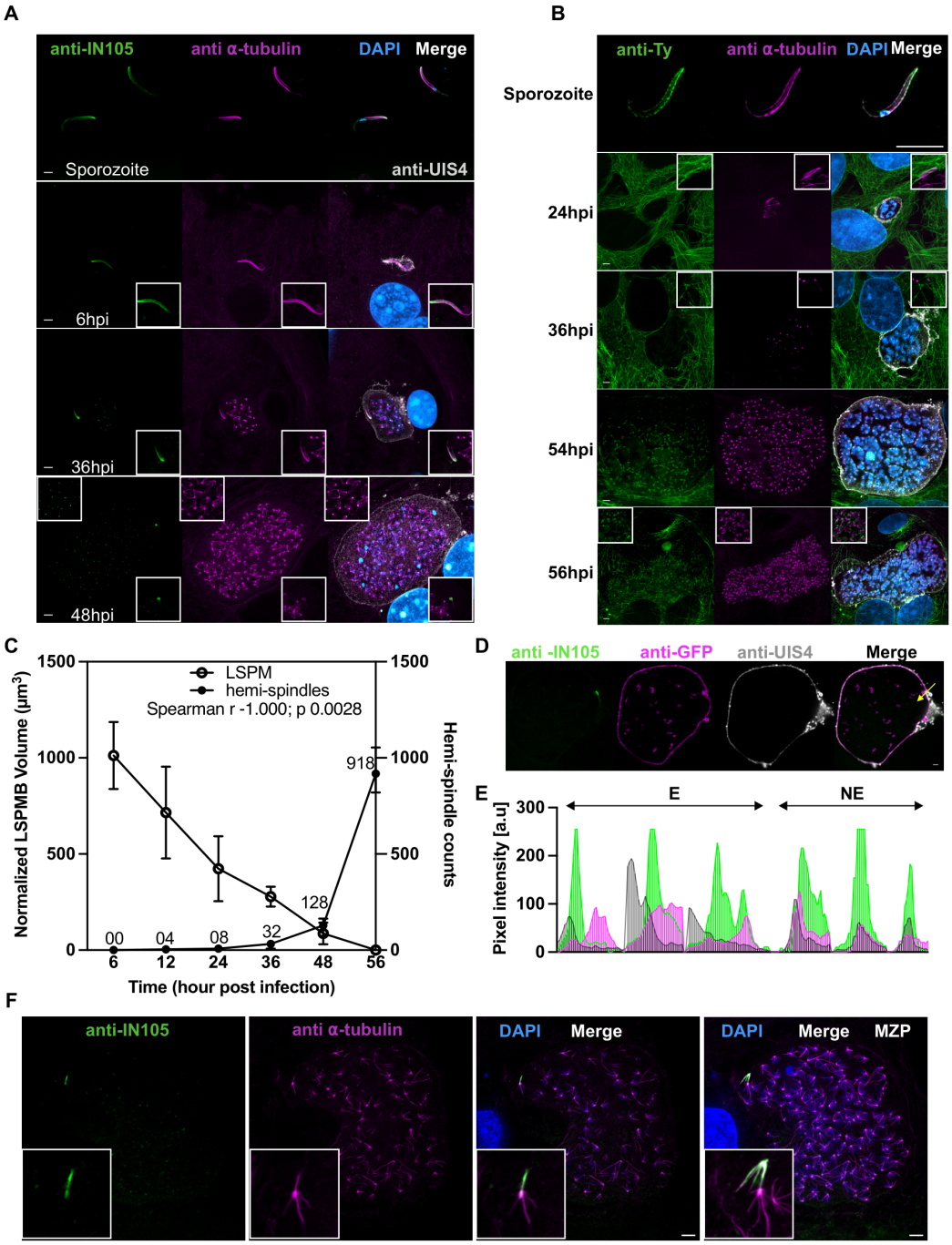
A
anti-IN105
anti α-tubulin
DAPI
Merge
Sporozoite
anti-UIS4
6hpi
36hpi
48hpi
B
anti-Ty
anti α-tubulin
DAPI
Merge
Sporozoite
24hpi
36hpi
54hpi
56hpi
C
LSPM
hemi-spindles
Spearman r -1.000; p 0.0028
Normalized LSPMB Volume (µm³)
Hemi-spindle counts
Time (hour post infection)
1500
1000
500
0
6
12
24
36
48
56
00
04
08
32
128
918
D
anti -IN105
anti-GFP
anti-UIS4
Merge
E
Pixel intensity [a.u]
300
200
100
0
E
NE
F
anti-IN105
anti α-tubulin
DAPI
Merge
DAPI
Merge
MZP

1005

1006 **Figure 3:** LSPMB is polyglutamylated
1007 **(A** and **B)** show maximum projection of confocal z-stacks form sporozoites and infected primary
1008 hepatocytes at different time points during liver stage development. Primary hepatocytes were
1009 isolated from mice and infected with sporozoites. Cells were fixed and stained with antibodies against
1010 **(A)** polyglutamylated tubulin (anti-IN105), **(B)** tyrosinated tubulin (anti-Ty), and α-tubulin (anti-α-
1011 tubulin). Nuclei were stained with DAPI (blue), and the PVM with anti-UIS4 (grey). ROIs in **(A)** show
1012 the LSPMB at 6 and 36 hpi and polyglutamylated hemi-spindle poles at 48 hpi. ROIs in (B) display
1013 LSPMB and α-tubulin evolution across liver stages. **(C)** Normalized LSPMB volume and the hemi-
1014 spindle pole counts from 6 hpi to 56 hpi, quantified using IMARIS 3D/4D analysis. LSPMB volume
1015 decreased from 1038.9 μm^3 at 6 hpi to 0 μm^3 at 56 hpi, while hemi-spindle poles count increased from
1016 0 at 6 hpi to a median of 928 at 56 hpi, showing a perfect Spearman anti-correlation coefficient of -1.
1017 n = 15 per time point. **(D)** Single-plane PS-ExM confocal image of infected HeLa cells at 36 hpi with
1018 parasites expressing PMP1::GFP. Cells were PFA-fixed and stained with anti-GFP (magenta), anti-
1019 IN105 (green), and anti-UIS4 (PVM). The yellow arrow indicates the direction of Cell RGB Profiler
1020 analysis from outside the PVM to inside the parasite. **(E)** Pixel intensity profiles (arbitrary units) for
1021 PVM (grey), LSPMB (green), and parasite plasma membrane (magenta) in expanded (PS-ExM) cells
1022 (E) and non-expanded (NE) cells. Overlap was observed in NE cells, while PS-ExM resolved LSPMB
1023 localization between the PVM and the parasite plasma membrane. n=10, in triplicate. Scare bar: 10
1024 µm. **(F)** Single-plane confocal image of infected primary hepatocytes fixed with cold methanol. Cells
1025 were stained with anti-IN105 (green), α-tubulin (magenta), and DAPI (blue). The ROI shows a LSPMB
1026 tubule in direct contact with a parasite hemi-spindle pole. MZP: Maximum Z projection. Scale bars: 10
1027 µm.

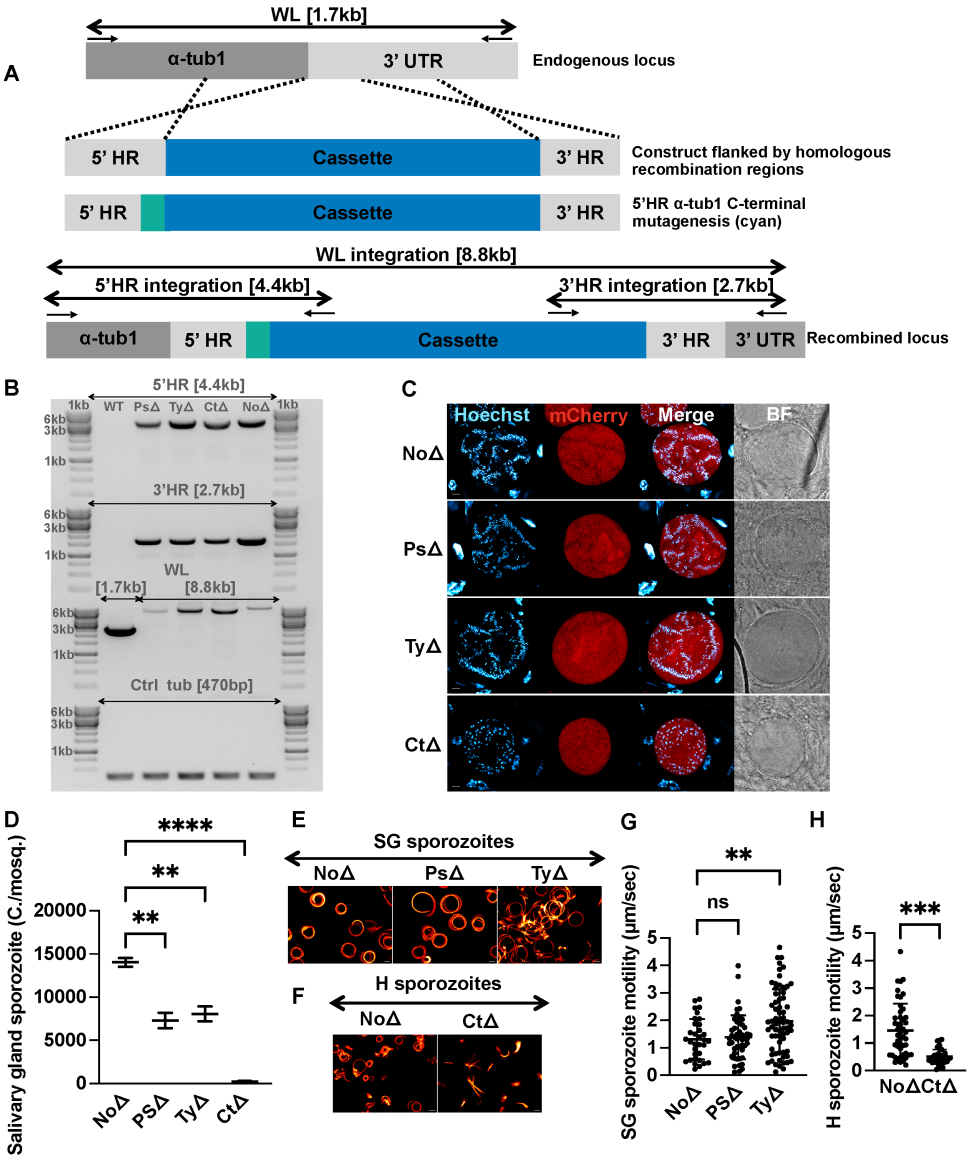
A
WL [1.7kb]
α-tub1
3' UTR
Endogenous locus
5' HR
Cassette
3' HR
Construct flanked by homologous recombination regions
5' HR
Cassette
3' HR
5'HR α-tub1 C-terminal mutagenesis (cyan)
WL integration [8.8kb]
5'HR integration [4.4kb]
3'HR integration [2.7kb]
α-tub1
5' HR
Cassette
3' HR
3' UTR
Recombined locus
B
5'HR [4.4kb]
WT PsΔ TyΔ CtΔ NoΔ
3'HR [2.7kb]
WL
[1.7kb]
[8.8kb]
Ctrl tub [470bp]
C
Hoechst
mCherry
Merge
BF
NoΔ
PsΔ
TyΔ
CtΔ
D
Salivary gland sporozoite (C./mosq.)
NoΔ
PSΔ
TyΔ
CtΔ
E
SG sporozoites
NoΔ
PsΔ
TyΔ
F
H sporozoites
NoΔ
CtΔ
G
SG sporozoite motility (µm/sec)
ns
NoΔ
PSΔ
TyΔ
H
H sporozoite motility (µm/sec)
NoΔCtΔ

Figure 4: *Plasmodium* α1-tubulin C-terminal post-translational modification is important for the mosquito stage development. **(A)** Schematic of the double homologous recombination (DHR) construct targeting the *Plasmodium* α1-tubulin gene (PBANKA_0417700) for C-terminal mutagenesis. The cassette (blue box) includes the 3'UTR *P. berghei* dihydrofolate reductase (PbDHFR), elongation factor-1 alpha (ef1α) promoter, human dihydrofolate reductase (hdhfr), yeast FCU (yfcu), 3'UTR PbDHFR, Hsp70 promoter, mCherry and the 3' UTR Hsp70, with the 3'UTR region of the PBANKA_0417700 gene. This cassette was flanked by a 5′ homologous region (5′HR) containing the α1-tubulin coding region including the stop codon (with introduced mutations in the C-terminal region, cyan box) and a part of the 3′UTR of the gene (3'HR). The construct was transfected into the PbWT (*P. berghei* ANKA line cl15cy1). Black arrows indicate PCR primer binding sites and expected product sizes. Primer sequences are listed in Table 2 and 3. **(B)** Integration PCR results for the mutant parasite lines, showing expected band sizes on a 1% agarose gel: 5'HR = 4.4 kb, 3'HR = 2.7 kb, whole locus (WL) = 8.8 kb. Ladder: 1 kb DNA marker. Genotypes: WT, (wild-type); PsΔ (glutamine-to-alanine substitution); TyΔ (deletion the C-terminal tyrosination/detyrosination residues); CtΔ (complete C-terminal deletion), and NoΔ (construct control with no mutation). To ensure that all samples contained the same amount of DNA, a control gene representing a portion of tubulin (Ctrl tub about 470 bp) was used for integration PCR. **(C)** Representative confocal images of live oocysts at 11 days post infection (dpi). Nuclei were stained with Hoechst 33342 (hot cyan) and cytosolic mCherry (red) was expressed under the HSp70 promoter. BF, brightfield. **(D)** Normalized salivary sporozoite counts at 18 dpi. The control (NoΔ) averaged 14,033 sporozoites count per mosquito (C./mosq.), compared to 7,300 (PsΔ), 8,066 (TyΔ), and 200 (CtΔ). Experiment performed in triplicate; n = 20 per replicate. **(E** and **F)** Wide-field microscope motility assay images of salivary gland sporozoites showing the typical circular movement (maximum z projection in Fiji) of the control, PsΔ, and TyΔ salivary gland (SG) sporozoites **(E)** and the control and CtΔ hemolymph (H) sporozoites **(F)**. For CtΔ, hemolymph sporozoites were used due to the absence of salivary gland sporozoites; these lacked typical motility. **(G))** Quantification of sporozoite gliding velocity for PsΔ, and TyΔ salivary gland sporozoites. Mean velocities: NoΔ = 1.3 μm/s, PsΔ = 1.38 μm/s, TyΔ = 1.9 μm/s, CtΔ = 0.5 μm/s. Statistical analysis: one-way ANOVA with Dunnett's multiple comparisons test (*$p \leq 0.05$, **$p \leq 0.01$, ***$p \leq 0.001$). **(H)** Quantification of sporozoite gliding velocity of CtΔ haemolymph sporozoites. The average gliding speed for control hemolymph sporozoites was 1.4 μm/s, whereas CtΔ sporozoites exhibited a slower speed of 0.5 μm/s. Statistical comparison tests were performed using two tailed unpaired t tests (*$p \leq 0.05$, **$p \leq 0.01$, ***$p \leq 0.001$).

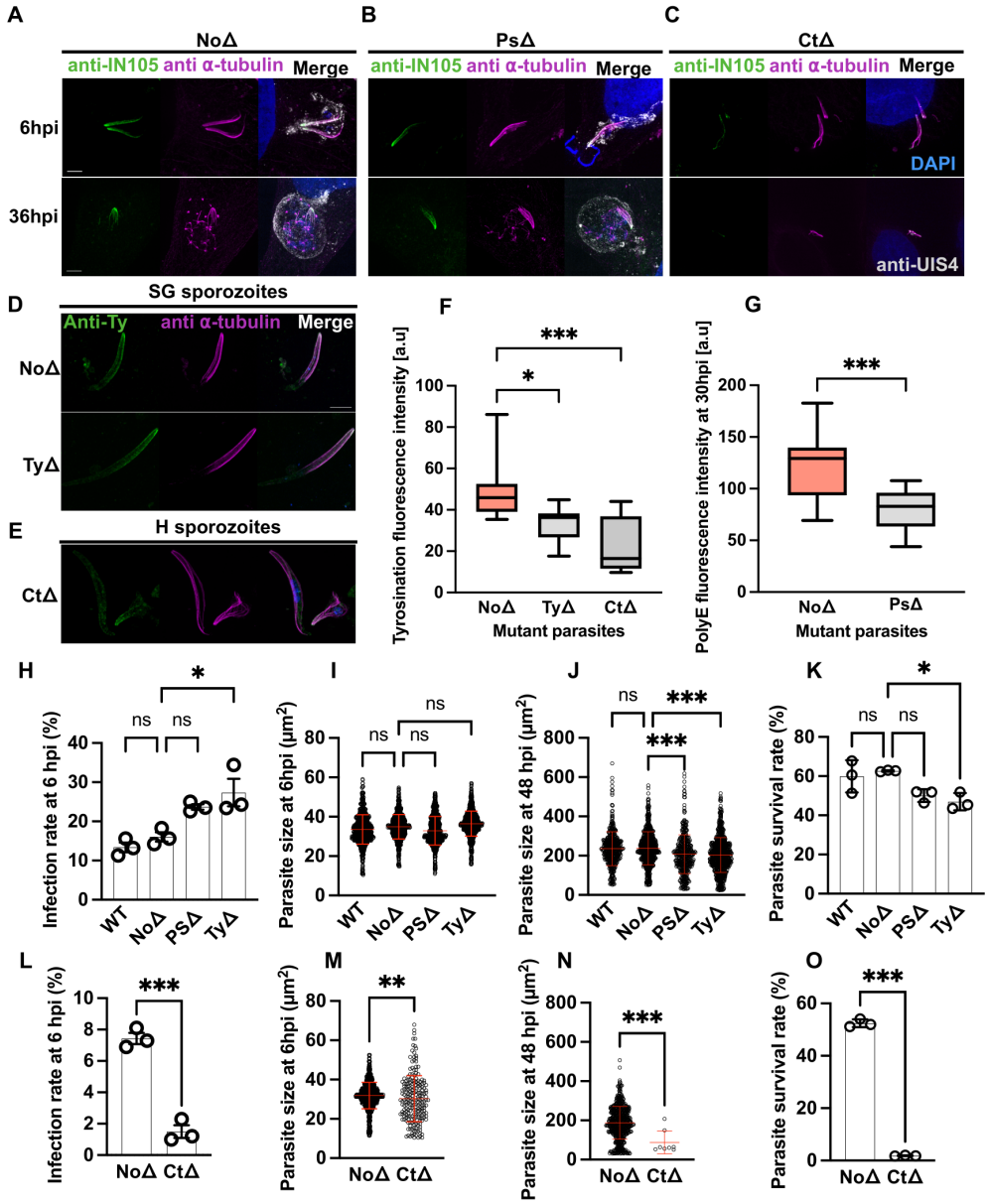
A
NoΔ
anti-IN105 anti α-tubulin Merge
6hpi
36hpi
B
PsΔ
anti-IN105 anti α-tubulin Merge
C
CtΔ
anti-IN105 anti α-tubulin Merge
DAPI
anti-UIS4
D
SG sporozoites
Anti-Ty anti α-tubulin Merge
NoΔ
TyΔ
E
H sporozoites
CtΔ
F
Tyrosination fluorescence intensity [a.u]
Mutant parasites
NoΔ TyΔ CtΔ
G
PolyE fluorescence intensity at 30hpi [a.u]
Mutant parasites
NoΔ PsΔ
H
Infection rate at 6 hpi (%)
ns ns *
WT NoΔ PSΔ TyΔ
I
Parasite size at 6hpi (μm²)
ns ns ns
J
Parasite size at 48 hpi (μm²)
ns *** ***
K
Parasite survival rate (%)
ns ns *
L
Infection rate at 6 hpi (%)
***
NoΔ CtΔ
M
Parasite size at 6hpi (μm²)
**
N
Parasite size at 48 hpi (μm²)
***
O
Parasite survival rate (%)
***

1062 **Figure 5**: Liver stage development of *Plasmodium* α1-tubulin mutant parasites.
1063 **(A, B** and **C)** Maximum projections of PS-ExM-acquired z-stack confocal images of infected HeLa
1064 cells at 6 and 36 hpi, showing the control (NoΔ), PsΔ, and CtΔ mutant parasites. **(D and E)** Maximum
1065 projections of PS-ExM-acquired z-stack confocal images of control and TyΔ salivary gland sporozoites,
1066 as well as CtΔ hemolymph sporozoites (E). In **(A, B and C)**, cells were stained with antibodies against
1067 polyglutamylated tubulin (anti-IN105), while **(D and E)** antibodies against tyrosinated tubulin (anti-Ty)
1068 were used. In all panels, α-tubulin was labeled with anti-α-tubulin, nuclei with DAPI (blue), and the
1069 parasitophorous vacuole membrane (PVM) with anti-UIS4 (grey). **(F** and **G)** represent the
1070 fluorescence intensity (arbitrary units, a.u.) of anti-Ty in sporozoites (F) and anti-IN105 at 36 hpi in the
1071 liver stage (G). In **(F)**, the mean fluorescence intensity of CtΔ (22 a.u.) was significantly reduced
1072 compared to TyΔ (33.4 a.u.) and NoΔ (49.6 a.u.), while in **(G)**, PsΔ (79.9 a.u.) showed a significant
1073 reduction compared to NoΔ (121 a.u.). **(H** and **L)** showed infection rates of mutant parasites in HeLa
1074 cells at 6 hpi, determined by pre-counted sporozoites and quantitative microscopy. PsΔ (23.7%) and
1075 TyΔ (27.3%) exhibited typical infection rates compared to control (NoΔ) (16%) and WT (14%) (H),
1076 whereas CtΔ hemolymph sporozoites had a drastically reduced infection rate (2%) relative to controls
1077 hemolymph sporozoites (7.4%) (L). **(K** and **O)** Parasite survival from 6 to 48 hpi, normalized to 100%
1078 at 6 hpi. At 48 hpi, survival rates were 63% (NoΔ), 60% (WT), 50% (PsΔ), and 47% (TyΔ) (K). In
1079 contrast, CtΔ hemolymph sporozoites showed a significantly lower survival rate (2%) compared to
1080 controls (52%) (O), indicating impaired viability. (**I** and **J, M** and **N)** Parasite size measurements at 6
1081 and 48 hpi for control, PsΔ, and TyΔ salivary gland sporozoites (I and J), as well as control and CtΔ
1082 hemolymph mutants (M and N). At 48 hpi, PsΔ (208.16 μm²) and TyΔ (203.7 μm²) were significantly
1083 smaller than NoΔ (237.9 μm²) and WT (235.7 μm²) (J). The CtΔ hemolymph mutants failed to establish
1084 liver stage infection, with an average size (88.1 μm²) markedly smaller than controls (187.4 μm²) (N).
1085 Each dot represents an individual parasite. PsΔ: Glutamine-to-alanine substitution at the
1086 polyglutamylation site; TyΔ: Deletion of C-terminal tyrosination/detyrosination residues; CtΔ:
1087 Complete deletion of PBANKA_0417700 α-tubulin C-terminal PTM residues and NoΔ: Control
1088 construct with no mutation. WT: wild type parasite. The experiments were conducted using, **(F, H, I, J,**
1089 **K)**: One-way ANOVA with Dunnett's multiple comparisons test (*$p \leq 0.05$, **$p \leq 0.01$, ***$p \leq 0.001$). **(G,**
1090 **L, M, N, O)**: Two-tailed unpaired t-tests (*$p \leq 0.05$, **$p \leq 0.01$, ***$p \leq 0.001$). All experiments were
1091 performed in triplicate.

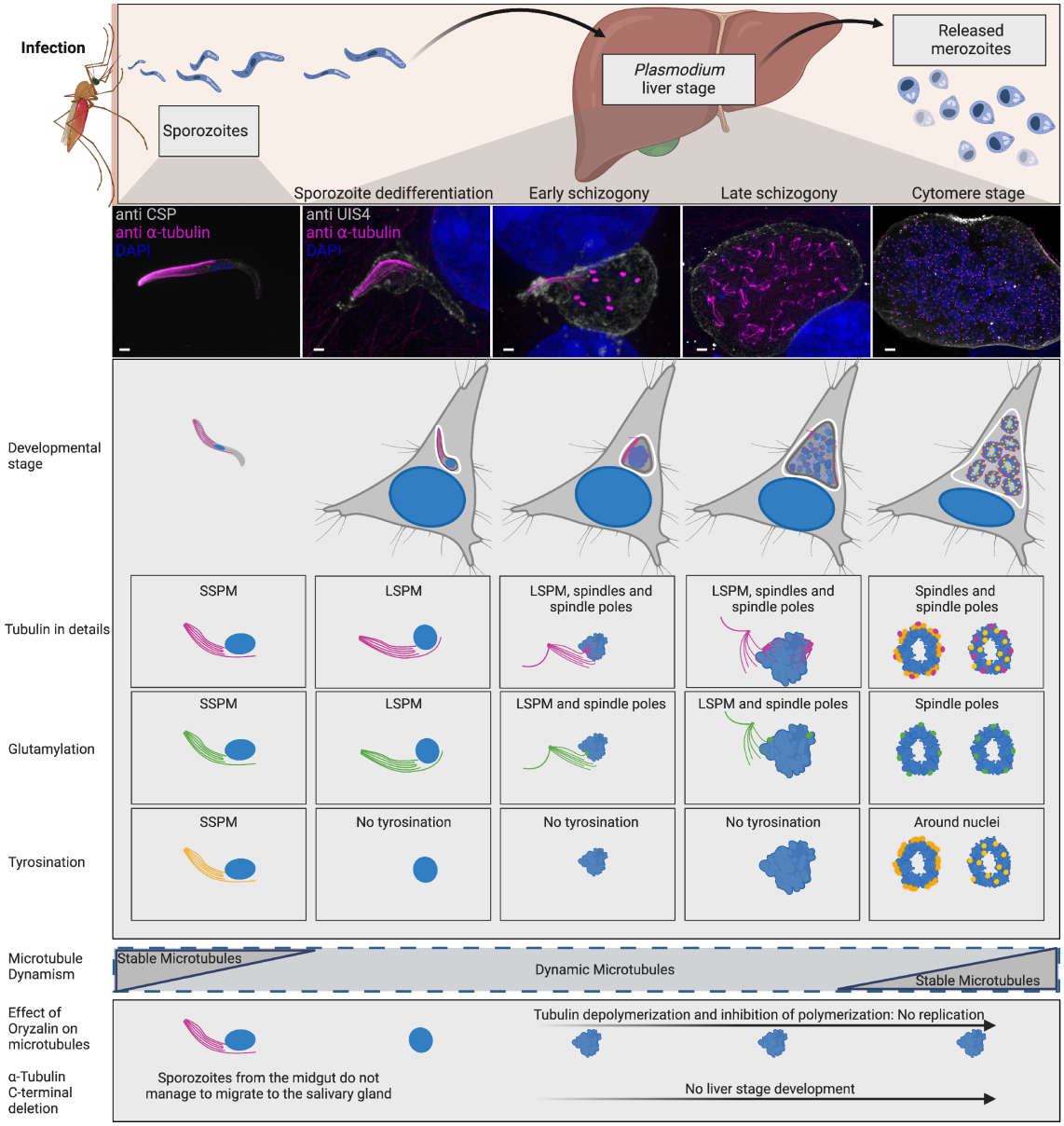
Infection
Sporozoites
Plasmodium liver stage
Released merozoites
Sporozoite dedifferentiation
Early schizogony
Late schizogony
Cytomere stage
anti CSP
anti α-tubulin
DAPI
anti UIS4
anti α-tubulin
DAPI
Developmental stage
Tubulin in details
SSPM
LSPM
LSPM, spindles and spindle poles
LSPM, spindles and spindle poles
Spindles and spindle poles
Glutamylation
SSPM
LSPM
LSPM and spindle poles
LSPM and spindle poles
Spindle poles
Tyrosination
SSPM
No tyrosination
No tyrosination
No tyrosination
Around nuclei
Microtubule Dynamism
Stable Microtubules
Dynamic Microtubules
Stable Microtubules
Effect of Oryzalin on microtubules
Tubulin depolymerization and inhibition of polymerization: No replication
α-Tubulin C-terminal deletion
Sporozoites from the midgut do not manage to migrate to the salivary gland
No liver stage development

1092

Figure 6: Model of the tubulin behavior during Plasmodium berghei salivary gland sporozoite and exo-erythrocytic stage.

The graphical abstract summarizes the key finding of this study.

It illustrates the development of *Plasmodium* parasites within primary hepatocytes, from invasion to the cytomere stage. α-tubulin was stained with anti-α-tubulin (magenta), nuclei with DAPI (blue), and the parasitophorous vacuole membrane (PVM) with anti-UIS4 (grey). The model highlights the evolution of sporozoite subpellicular microtubules (SSPM) into liver stage subpellicular microtubules (LSPMB), along with their associated tubulin post-translational modifications (PTMs). We propose that polyglutamylated LSPMB originates from the SSPM and is recycled during liver stage development to support hemi-spindle pole formation, membrane biogenesis, and potentially other functions. Upon hepatocyte invasion, the SSPM loses tyrosination, a modification that initially confers stability and supports sporozoite motility. This detyrosination likely facilitates parasite shape transformation, increases microtubule dynamics, and enables interactions with ER structures and MAPs. Tyrosination reappears in late stages, possibly stabilizing merozoite microtubules for erythrocyte invasion. Microtubule-stabilizing drugs did not affect the SSPM but inhibited liver stage microtubule polymerization, confirming their dynamic nature. Inhibition of microtubule dynamics also prevented merozoite formation. Finally, C-terminal tubulin PTM residues were shown to be essential for salivary gland sporozoite development and successful liver stage infection.

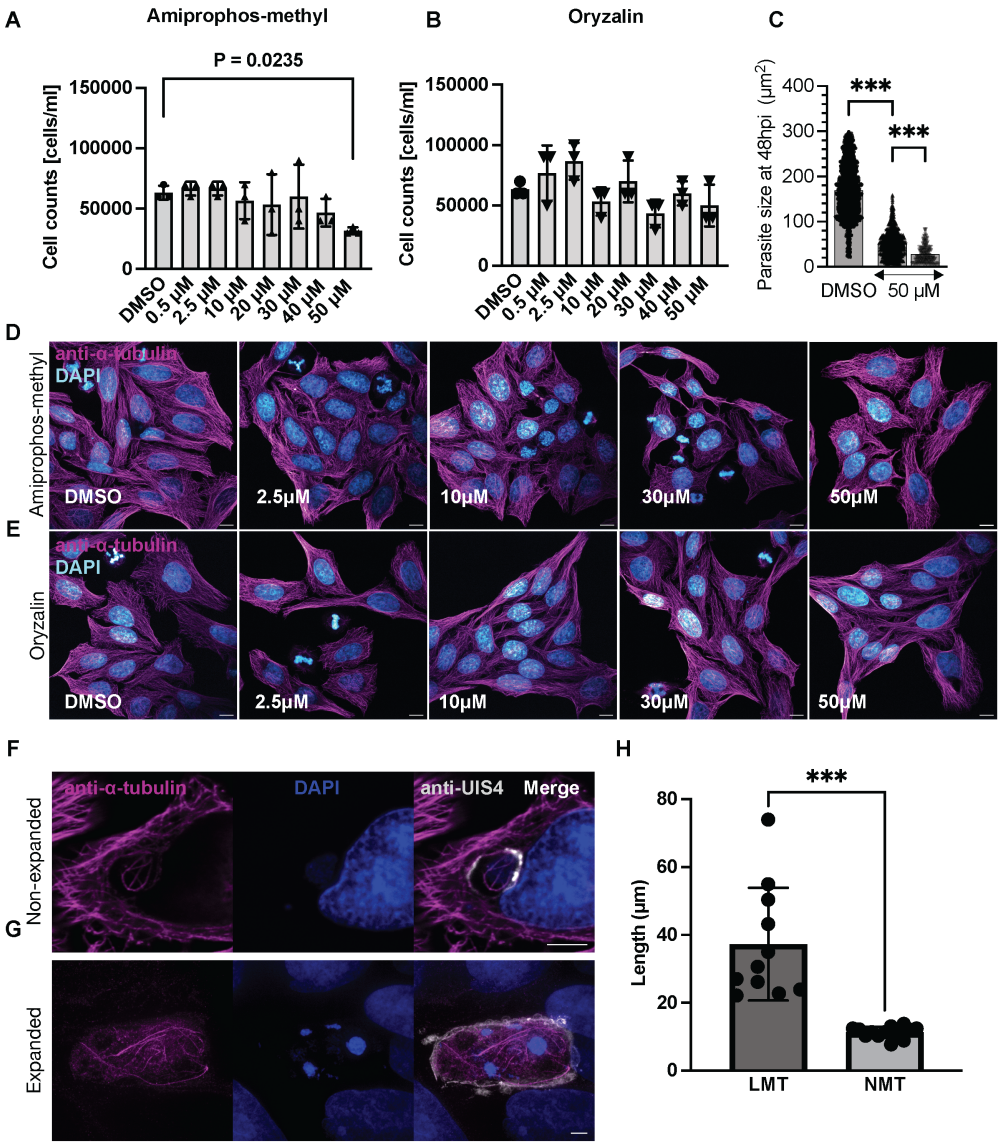
A
Amiprophos-methyl
P = 0.0235
Cell counts [cells/ml]
150000
100000
50000
0
DMSO
0.5 µM
2.5 µM
10 µM
20 µM
30 µM
40 µM
50 µM
B
Oryzalin
Cell counts [cells/ml]
C
Parasite size at 48hpi (µm2)
400
300
200
100
0
***
***
DMSO
50 µM
D
Amiprophos-methyl
anti-α-tubulin
DAPI
DMSO
2.5µM
10µM
30µM
50µM
E
Oryzalin
anti-α-tubulin
DAPI
DMSO
2.5µM
10µM
30µM
50µM
F
Non-expanded
anti-α-tubulin
DAPI
anti-UIS4
Merge
G
Expanded
H
***
Length (µm)
80
60
40
20
0
LMT
NMT

1111

1112
1113 **S1 Figure** Effect of *Plasmodium*-specific microtubule inhibitors on HeLa cells
1114 HeLa cells were seeded in 6-well plates and treated the following day with various concentrations of
1115 microtubule-targeting drugs. Media were replaced daily with fresh drug-supplemented medium. After
1116 five days, surviving cells were detached and counted. **(A)** Effect of amiprophos-methyl (AMP) on HeLa
1117 cell viability. A significant reduction in cell count was observed only at 50 μM compared to the DMSO
1118 control. **(B)** effect of the oryzalin on HeLa cells viability. No significant differences in cell count were
1119 observed at any tested concentrations tested relative to DMSO. **(C)** represent the parasite size at 48
1120 hpi in infected HeLa cells treated with oryzalin and AMP at 50 μM. oryzalin showed a significant
1121 inhibitory effect on parasite growth compared to AMP and DMSO control. Statistical comparison tests
1122 were performed using a one-way ANOVA test (*$p \leq 0.05$, **$p \leq 0.01$, ***$p \leq 0.001$). **(D** and **E)** Maximum
1123 projection confocal IFA z-stacks of HeLa cells treated with amiprophos-methyl (D) and oryzalin (E)
1124 tested at different concentrations, respectively. Cells were fixed with cold and stained with anti-α-
1125 tubulin (magenta) and DAPI (blue). **(F)** Confocal IFA z-projection of HeLa cells treated with low-dose
1126 oryzalin (0.5 μM), showing unusually elongated microtubule structures. **(G)** PS-ExM confocal z-stack
1127 of oryzalin-treated cells showing the very long LSPMB and hemi-spindles. **(H)** Quantification of
1128 LSPMB and hemi-spindle lengths. Oryzalin-treated microtubules were on average four times longer
1129 than those in DMSO-treated controls. Each dot represents a measurement from a single cell. LMT,
1130 Long microtubule; NMT, normal microtubule. Statistical comparison tests were performed using two
1131 tailed unpaired t tests (*$p \leq 0.05$, **$p \leq 0.01$, ***$p \leq 0.001$).

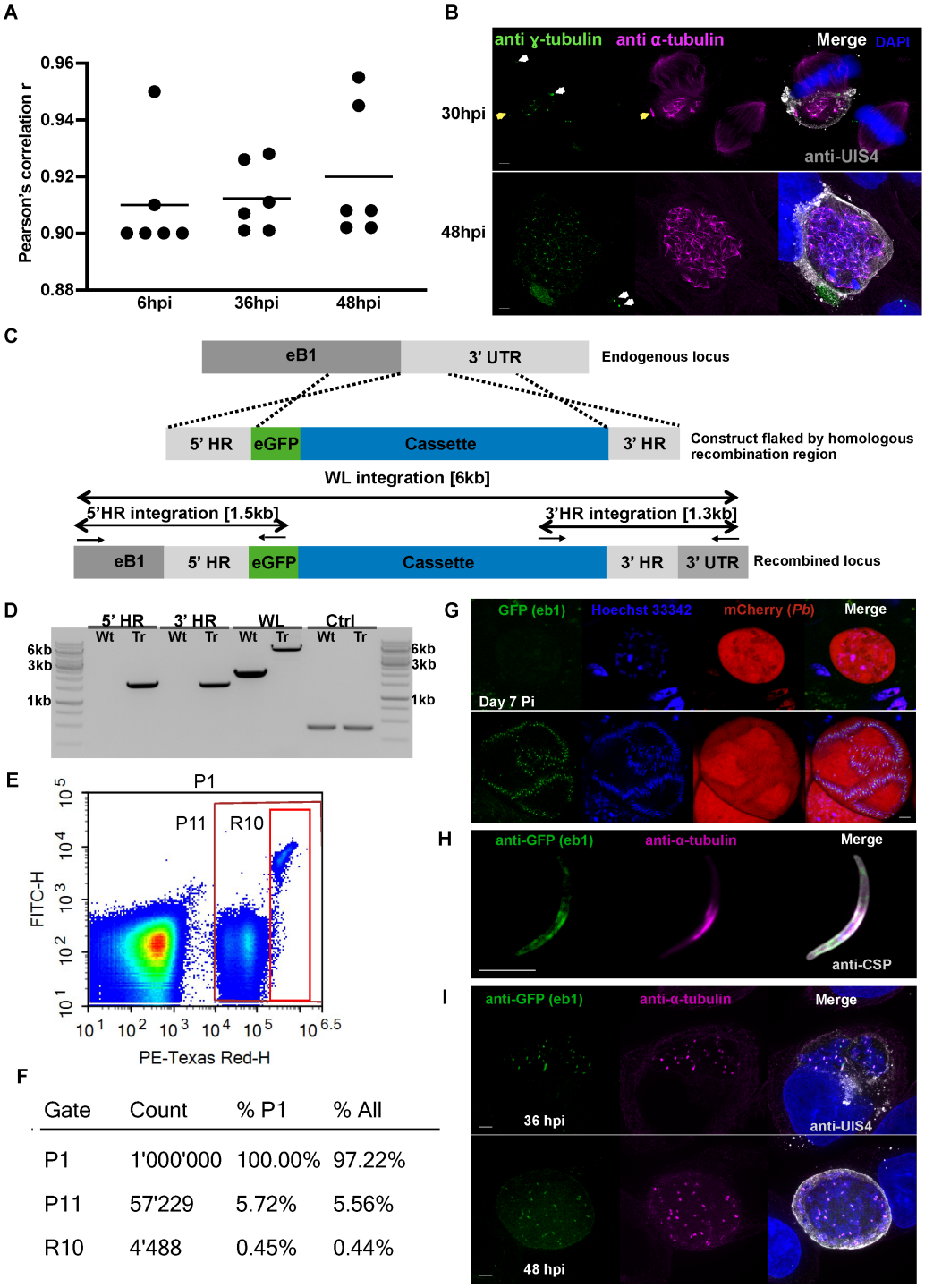
A
Pearson's correlation r
0.96
0.94
0.92
0.90
0.88
6hpi
36hpi
48hpi
B
anti γ-tubulin
anti α-tubulin
Merge
DAPI
30hpi
anti-UIS4
48hpi
C
eB1
3' UTR
Endogenous locus
5' HR
eGFP
Cassette
3' HR
Construct flaked by homologous recombination region
WL integration [6kb]
5'HR integration [1.5kb]
3'HR integration [1.3kb]
eB1
5' HR
eGFP
Cassette
3' HR
3' UTR
Recombined locus
D
5' HR
3' HR
WL
Ctrl
Wt
Tr
6kb
3kb
1kb
E
P1
P11
R10
FITC-H
PE-Texas Red-H
F
Gate Count % P1 % All
P1 1'000'000 100.00% 97.22%
P11 57'229 5.72% 5.56%
R10 4'488 0.45% 0.44%
G
GFP (eb1)
Hoechst 33342
mCherry (Pb)
Merge
Day 7 Pi
H
anti-GFP (eb1)
anti-α-tubulin
Merge
anti-CSP
I
anti-GFP (eb1)
anti-α-tubulin
Merge
36 hpi
anti-UIS4
48 hpi

S2 Figure *Plasmodium* end-binding protein 1 (eB1) is expressed in mosquito and liver stage **(A)** Pearson correlation coefficients between polyglutamylated LSPMB and α-tubulin LSPMB at 6, 36, and 48 hpi during liver stage development. On average, 92% of polyglutamylated tubulin colocalized with the LSPMB. **(B)** Maximum projection of PS-ExM confocal z-stacks of infected HeLa cells fixed at 30 and 48 hpi. Cells were stained with anti-γ-tubulin (green), anti-α-tubulin (magenta), anti-UIS4 (grey, PVM), and DAPI (blue, nuclei). White arrows indicate host centrosomes; yellow arrows highlight the LSPMB. Parasite hemi-spindle poles were also detected with γ-tubulin. **(C)** Schematic of the double homologous recombination construct used to tag *Plasmodium* eB1 (PBANKA_0405600) with eGFP at the C-terminus. The expression cassette (blue box) includes 3′UTR *Pb*DHFR, EF1α promoter, hDHFR, yeast fcu, and the 3′UTR of PBANKA_0405600, flanked by the 5′HR (eB1 coding region) and 3′UTR. The construct was transfected into the PbmCherry 1868 mother line. **(D)** Integration PCR confirming correct insertion of the eGFP-tagged eB1 cassette. PCR product sizes: 5′HR = 1.5 kb, 3′HR = 1.3 kb, whole locus (WL) = 6 kb. Primer sequences listed in Table 1. Lane labels: Tr (transgenic), WT (wild type), ctrl (control). Ladder: 1 kb DNA marker. **(E)** Flow cytometry profile of erythrocytes infected with eB1-GFP-expressing parasites. Gate P1 includes all analyzed cells; P11 identifies mCherry-positive (PE-Texas Red-H) infected erythrocytes; R10 identifies GFP+/mCherry+ gametocytes. **(F)** Summary table showing parasitemia percentages across gates defined in (E). **(G)** Representative confocal live imaging of *P. berghei* eB1-GFP oocysts at 7 and 12 days post-infection (dpi), showing eB1-GFP (green), parasite mCherry (red), and Hoechst-stained nuclei (blue). Scale bar: 5 μm. **(H)** Confocal IFA image of *P. berghei* eB1-GFP sporozoites stained with anti-GFP (green), anti-α-tubulin (magenta), and anti-circumsporozoite protein (CSP, grey). **(I)** Maximum projection of PS-ExM confocal z-stacks of HeLa cells infected with *P. berghei* eB1-GFP parasites at 36 and 48 hpi. Cells were stained with anti-GFP (green), anti-α-tubulin (magenta), and anti-UIS4 (grey). Scale bar: 10 μm.

A

- Residue 40 (K40) where Acetylation happens
- C-terminal (Y, tyrosinated and E, Detyrosinated)
- Residue where polyglutamylation happens

>XP_034420234.1 alpha tubulin 1 [*Plasmodium berghei ANKA*] 453aa

MREVISIHVGQAGIQVGNACWELFCLEHGIQPDGQMPPDQAGRANDDAFNTFFSETGAGKHVPRCVFVDL
EPTVVDEVRTGTYRQLFHPEQLISGKEDAANNFARGHYTIGKEVIDVCLDRIRKLADNCTGLQGFLMFSA
VGGGTGSGFGCLMLERLSVDYGKKSKLNFCCWPSPQVSTAVVEPYNSVLSTHSLLEHTDVAIMLDNEAIY
DICKKNLDIERPTYTNLNRLIAQVISSLTASLRFDGALNVDVTEFQTNLVPYPRIHFMLSSYAPVVSAEK
AYHEQLSVSEITNSAFEPANMMAKCDPRHGKYMACCLMYRGDVVPKDVNAAVATIKTKRTIQFVDWCPTG
FKCGINYQPPTVVPGGDLAKVMRAVCMISNSTAIAEVFSRMDQKFDLMYAKRAFVHWYVGEGMEEGEFSE
AREDLAALEKDYEEVGIETNDGEGEDEGYEADY

>XP_034420468.1 alpha tubulin 2 [*Plasmodium berghei ANKA*] 450aa

MREVISIHVGQAGIQIGNACWELFCLEHGIQPDGQMPSDQVVAGGDDAFNTFFSETGAGKHVPRCVFVDL
EPTVVDEVRTGTYRQLFHPEQLISGKEDAANNFARGHYTIGKEIVDICLDRVRKLADNCTGLQGFLMFNA
VGGGTGSGLGCLLLERLAIDYGKKSKLNFCSWPSPQVSTAVVEPYNSVLSTHSLLEHTDVAIMLDNEAIY
DICKKNLDIERPTYTNLNRLIAQVISSLTASLRFDGALNVDVTEFQTNLVPYPRIHFMLSSYAPIISAEK
AYHEQLSVSEITNSAFEPASMMAKCDPRHGKYMACCLMYRGDVVPKDVNAAVATIKTKRSIQFVDWCPTG
FKCGINYQPPTVVPGGDLAKVMRAVCMISNSTAIAEVFSRMDQKFDLMYAKRAFVHWYVGEGMEEGEFSE
AREDLAALEKDYEEVGIETNDGEGEDEGYE

B

2059

Pb PBANKA_0417700.	GAAACAAATGATGGCGAAGGAGAAGATGAAGGATATGAGGCAGACTATTAA
Pb PBANKA_0417700 No"	GAAACAAATGATGGCGAAGGAGAAGATGAAGGATATGAGGCAGACTATTAA
Pb PBANKA_0417700 Ps"	GAAACAAATGATGGCGAAGGAGCGGATGAAGGATATGAGGCAGACTATTAA
Pb PBANKA_0417700 Ty"	GAAACAAATGATGGCGAAGGAGAAGATGAAGGA----------TAA
Pb PBANKA_0417700 Ct"	GAAACAAATGATGGC----------TAA

C

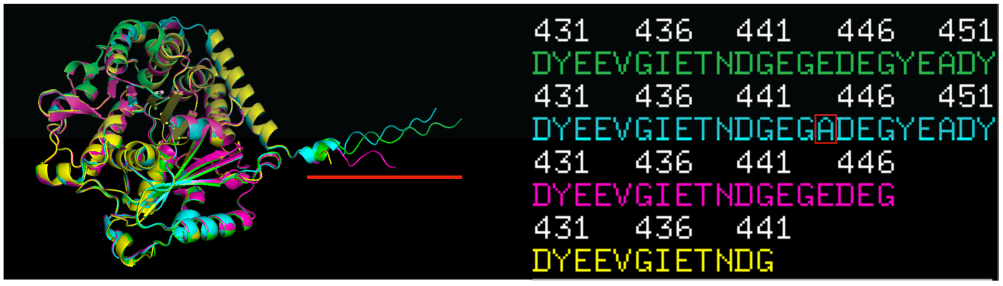

D

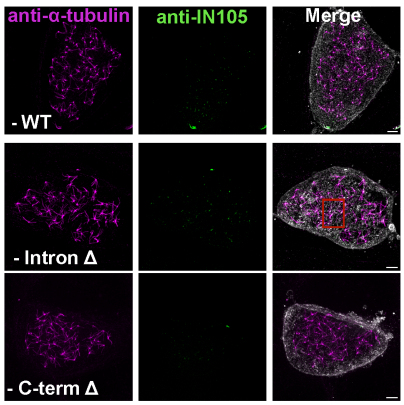

E

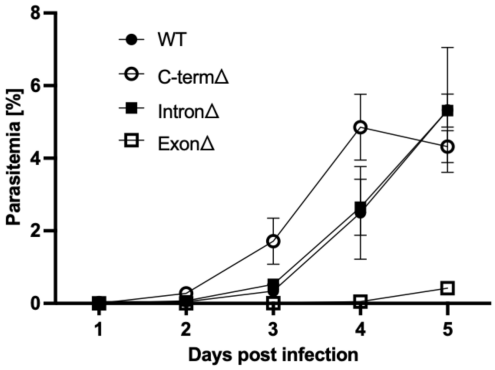

S3 Figure *Plasmodium* α-tubulin proteins and mutant parasite characterization.

(A) Comparison of *Plasmodium* α1- and α2-tubulin protein sequences highlighting predicted post-translational modification (PTM) sites. Polyglutamylation site E445 is conserved in both isoforms (green). α1-tubulin contains a predicted tyrosination site at Y453 (magenta), while α2-tubulin has a predicted detyrosination site at E450 (magenta). Neither isoform has the conserved acetylation site K40 (yellow). C-terminal PTM regions are underlined in red. **(B)** Sequence alignment of PBANKA_0417700 gene showing mutations introduced in the tubulin mutant parasites. Red highlights indicate substitutions or deletions. Dashes (—) indicate deleted nucleotides. Ps″: glutamine (E) substituted with alanine (A) at the polyglutamylation site; Ty″: deletion of the C-terminal tyrosination/detyrosination motif; Ct″: deletion of the entire C-terminal PTM region; No″: unmodified construct control. **(C)** Structural comparison of α1-tubulin mutant proteins using AlphaFold 3 predictions, aligned with PyMOL (Version 2.6.0). Green: wild type (No″); cyan: Ps″ mutant; magenta: Ty″ mutant; and yellow: Ct″ mutant. All predicted structures retained overall folding. **(D)** Maximum projection of confocal z-stacks of HeLa cells infected with mutant parasites (adapted from Freedy et al.). Microtubules were stained with anti-α-tubulin (magenta) and polyglutamylated tubulin with anti-IN105 (green). Nuclei were stained with DAPI (blue); the parasitophorous vacuole membrane (PVM) was stained with anti-UIS4 (grey). IntronΔ: line with deleted introns in the *Plasmodium* α1-tubulin gene; C-termΔ: line with deletion of C-terminal residues 540ADY. **(E)** In vivo infection kinetics in mice infected with mutant parasites. Parasitemia was measured daily from day 1 to day 5 post-infection. No significant differences were observed between mutant lines (intronΔ and C-termΔ) and wild type (WT). ExonΔ: mutant line in which α1-tubulin exons were replaced with α2-tubulin introns. This line failed to produce salivary gland sporozoites. Liver stage development in this line was delayed by 4 days due to hemolymph sporozoites used. Experiments were performed in triplicate.

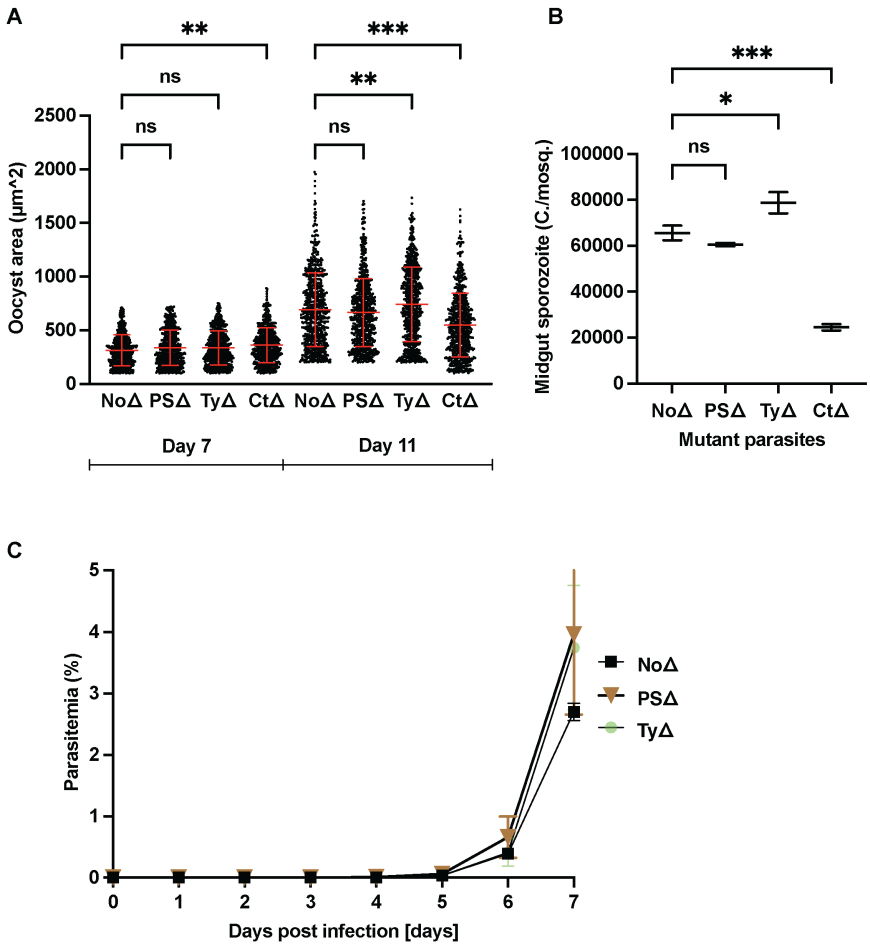
A
**
***
ns
**
ns
ns
2500
2000
1500
1000
500
0
Oocyst area (µm^2)
NoΔ PSΔ TyΔ CtΔ NoΔ PSΔ TyΔ CtΔ
Day 7
Day 11
B
***
*
ns
100000
80000
60000
40000
20000
0
Midgut sporozoite (C./mosq.)
NoΔ PSΔ TyΔ CtΔ
Mutant parasites
C
5
4
3
2
1
0
Parasitemia (%)
0 1 2 3 4 5 6 7
Days post infection [days]
NoΔ
PSΔ
TyΔ

1181

1182 **S4 Figure** Plasmodium α-tubulin mutant parasite oocyst formation and sporozoite infectivity.
1183 **(A)** Comparison of oocyst area at day 7 and 11 post-infection. No significant difference was observed
1184 between the WT (NoΔ) and the PsΔ or TyΔ mutants at day 7 post-infection. However, by day 11, the
1185 CtΔ mutant exhibited a significantly reduced oocyst size compared to the WT. **(B)** Normalized midgut
1186 sporozoites count per mosquito (C./mosq.) at day 14 post-feeding. No significant difference in
1187 sporozoite numbers was observed between NoΔ and PsΔ, whereas CtΔ showed a drastic reduction.
1188 In contrast, TyΔ displayed both a significantly larger oocyst size at day 11 and a higher sporozoite
1189 count at day 14 compared to the WT. **(C)** Blood parasitemia levels in mice infected with mutant
1190 parasites, measured from day 0 to day 7 post-infection. All mutants (PsΔ and TyΔ) established
1191 infections and progressed similarly to the WT (NoΔ). PsΔ: glutamine-to-alanine substitution at
1192 polyglutamylation site; TyΔ: deletion of C-terminal tyrosination/detyrosination residues; CtΔ: complete
1193 deletion of PBANKA_0417700 α-tubulin C-terminal PTM residues; NoΔ: control construct with no
1194 mutation. The experiments were conducted in triplicate. Statistical multiple comparisons were
1195 performed using one-way ANOVA with Dunnett's multiple comparisons test (*$p \leq 0.05$, **$p \leq 0.01$, ***p
1196 ≤ 0.001).

1197 **Movies**

1198 **Movie 1**: time-lapse live imaging of *P. bergei* salivary gland sporozoites expressing GFP cytosolically.
1199 Sporozoites were isolated and incubated with tubulin tracker SPY650. Microtubules are shown in
1200 magenta; sporozoites are shown in green. Scale bar: 5μm.

1201 **Movies 2, 3**, and **4**: Time-lapse live imaging of HeLa cells infected with *P. berghei* liver stage parasites
1202 expressing cytosolic GFP. Infected cells were incubated with tubulin tracker SPY650 for one hour
1203 prior to imaging. The movies show the development and dynamics of the LSPMB during liver stage
1204 infection. Microtubules are shown in magenta; parasites are shown in green. **Movie 2**: imaging from
1205 10 hpi to 25 hpi. **Movie 3:** imaging from 30 hpi to 35 hpi, and **Movie 4:** imaging from 37 hpi to 49 hpi.
1206 Scale bar: 5 μm.

1207 **Movies 5**, **6**, and **7** Time-lapse live imaging of HeLa cells infected with *P. berghei* liver stage parasites
1208 expressing cytosolic GFP. Infected cells were incubated with tubulin tracker SPY650 for one hour
1209 prior to imaging. The movies highlight the high dynamicity of the LSPMB during liver stage
1210 development, starting from early schizogony (~30 hpi). Microtubules are shown in magenta; parasites
1211 are shown in green. Scale bar: 5 μm.

1212 **Movies 8**, **9**, and **10** Time-lapse live imaging of HeLa cells infected with *P. berghei* liver stage
1213 parasites expressing cytosolic GFP. Infected cells were incubated with tubulin tracker SPY650 for one
1214 hour prior to imaging. The movies reveal the interaction between the LSPMB and the parasite's hemi-
1215 spindles and spindle poles during liver stage development. Microtubules are shown in magenta;
1216 parasites are shown in green. **Movie 8**: LSPMB (white arrow) localizes at the periphery of the parasite
1217 and connects to hemi-spindles. **Movie 9:** LSPMB (white arrows) connects to the parasite's hemi-
1218 spindle poles. **Movie 10:** shrinkage of the LSPMB during the liver stage development (ROI marked
1219 by a white arrow). Scale bar: 5 μm.

1220 **Supplementary Movie 1**: 3D projection of PS-ExM images showing LSPMB connected to the hemi-
1221 spindle pole in *P. berghei*-infected primary hepatocytes. Fixed and expanded primary hepatocytes
1222 were stained with anti-IN105 (polyglutamylated tubulin, green), anti-α-tubulin (magenta), and anti-
1223 UIS4 (PVM, grey). The movie shows the LSPMB in contact with the parasite's hemi-spindle pole.
1224 Image analysis was performed using IMARIS 3D and 4D visualization software.

1225 **Supplementary Movie 2:** *Plasmodium berghei* salivary gland (SG) sporozoite motility of *P. berghei*
1226 NoΔ (control), PsΔ, and TyΔ mutants, as well as hemolymph sporozoites of *P. berghei NoΔ* and CtΔ
1227 mutants. *Scale bar: 5 µm*

1228 **Tables**

1229 **Table 1:** *Plasmodium berghei* eB1egfp parasites integration PCR primer

Integration	Mutants	Primer pair	Primer Sequence	Expected size
5'HR		upstream of the construct	GGTTGTAAGTCGAAAAGAGCTGATAGAA	1.5kb
		within the ef1alpha	TCGATGCCCTTCAGCTCG	
3'HR		within yfcu	GAGGTGTTAAGCCAGAGAG	1.3kb
		downstream the 3'UTR	CGGTTCAATAAATGAGGGATTAGC	
Whole locus		Forward	GGTTGTAAGTCGAAAAGAGCTGATAGAA	6kb
		Reverse	CGGTTCAATAAATGAGGGATTAGC	
Control		Forward	TGGAGCAGGAAATAACTGGG	470bp
		Reverse	ACCTGACATAGCGGCTGAAA	

1230

1231 **Table 2:** *Plasmodium berghei* α1-tubulin mutant parasites integration PCR primer

Integration	Mutants	Primer pair	Primer Sequence	Expected size
5'HR	PsΔ TyΔ CtΔ NoΔ	upstream of the construct	CGTATGCTCTACGCACTTCGC	4.4kb
		within the ef1alpha	GGTGCTTTGAGGGGTGAGC	
3'HR	PsΔ TyΔ CtΔ NoΔ	within mCherry	CCTACAAGGCCAAGAAGC	2.7kb
		Within the 3'UTR	CCATGTTCCCATGTGTATCTAC	
Whole locus	PsΔ TyΔ CtΔ NoΔ	Forward	CGTATGCTCTACGCACTTCGC	8.8kb
		Reverse	CCATGTTCCCATGTGTATCTAC	
Control	PsΔ TyΔ CtΔ NoΔ	Forward	TGGAGCAGGAAATAACTGGG	470bp
		Reverse	ACCTGACATAGCGGCTGAAA	

1232

1233

1234

1235

1236

1237

1238

1239

1240 **Table 3:** *Plasmodium berghei* α1-tubulin mutagenesis QuickChangeII primers sequences

Method/Kits	Mutations	Primer pair	Primer Sequence
Mutagenesis/ QuickChangeII	PsΔ	Primer	GTCTGCCTCATATCCTTCATCCGCTCCTTCGCCATCATTTGTTTC
		antisense	GAAACAAATGATGGCGAAGGAGCGGATGAAGGATATGAGGCAGAC
	TyΔ	Primer	GTAAGAAAAACGGCGGCCTTATCCTTCATCTTCTCCTTCG
		antisense	CGAAGGAGAAGATGAAGGATAAGGCCGCCGTTTTTCTTAC
	CtΔ	Primer	GTAAGAAAAACGGCGGCCTTAGCCATCATTTGTTTCAATTCC
		antisense	GGAATTGAAACAAATGATGGCTAAGGCCGCCGTTTTTCTTAC

1241

1242